Review of the CH-STED performance and application range over conventional STED

Rafael Diaz

2000953

Master's Thesis
Åbo Akademi University
01.06.2023

Master's degree in Biomedical Imaging
Specialisation theme: STED super-resolution imaging

Credits: 40 ECTS
Supervisors:
1. Elena Tcarenkova M.Sc
2. Prof. Pekka Hänninen Ph.D.

Passed:
Grade:

Abstract

University of Turku

Department of Medical Physics and Engineering

Laboratory of Biophysics

Rafael Diaz: Review of the CH-STED performance and application range over conventional STED

Master’s thesis, 57 pp., Appendices, 3 pp.

STED super-resolution imaging

May 2023

Super resolution in fluorescence through Stimulated Emission Depletion has been a reality since the beginning of the century. However, improvement is always pursued as the resolution is dependent on the intensity of the depletion beam. Combinations of depletion beam modulating masks are often proposed, yet their superposition is usually incoherent, and tends to lead to incidence of fluorescence in the zero-intensity area. Enhancements to the commonly used STED phase masks may provide sharper depletion areas without the need to significantly increase the depletion beam intensity. Coherent-Hybrid STED (CH-STED) is one alternative based on the addition of a 2D-STED phase mask to a rescaled z-STED mask to create a bi-vortex for improving contrast and axial resolution on the final image. This study evaluates the reproducibility and performance of CH-STED.

The CH-STED mask was analyzed and modified to fit the existing STED microscope, despite certain setbacks. The manual and digital alignment of the depletion beam and the masks to ensure the zero-intensity area was performed with gold nanoparticles, taking advantage of their reflective property. Several samples, comprising of fluorescent beads and vimentin dyed in Mouse Embryonic Fibroblast cells, were subsequently imaged to provide optical sectioning and lateral resolution comparisons between 2D-STED and CH-STED.

The removal of out-of-focus elements in thick sections of the cell samples was observed using the CH-STED mask, compared to 2D-STED where, regardless of depth, the out-of-focus elements still appeared. Further analysis was performed on the nanoparticle images to quantitatively establish the extent of the background suppression, as well as the improvement in the axial resolution in cell samples.

Keywords: Super-resolution microscopy, Stimulated Emission Depletion microscopy, Coherent-Hybrid STED, Python

List of Abbreviations

2PE – Two-Photon Excitation

3PE – Three-Photon Excitation

AO – Adaptive Optics

APD – Avalanche Photo Diode

CW – Continuous Wave

CH-STED - Coherent-Hybrid Stimulated Emission Depletion Microscopy

FWHM – Full Width at Half Maxima

g-STED – Gated Stimulated Emission Depletion Microscopy

GUI – Graphical User Interface

ISM – Image Scanning Microscopy

LCD – Liquid Crystal Display

LCOS – Liquid Crystal On Silicon

MEF – Mouse Embryonic Fibroblast

NA – Numerical Aperture

NPs – Nanoparticles

PMT – Photo Multiplier Tube

PSF – Point Spread Function

RESOLFT - REversible Saturable OpticaL Fluorescence Transitions

SE – Stimulated Emission

SLM – Spatial Light Modulator

SNR – Signal to Noise Ratio

STED – Stimulated Emission Depletion

Table of Contents

1. BACKGROUND

Light microscopy is an imaging technique by which an image of a sample is created through the merging of light diffracted by the sample, the interference of the light rays, and their collection by an objective lens. This imaging setup is known as Widefield Microscopy, where the detection is throughout the field of view of the objective. Alternatively, the imaging setup for Confocal Microcopy provides optical sectioning along with its point scanning detection configuration. The details we are able to distinguish in the resulting image, if possible, are restricted by the resolution of the microscopy system (Verdaasdonk et al., 2014).

1.1. Imaging characteristics of Optical Systems

1.1.1. Resolution

The natural property of diffraction of light prevents rays from converging into one specific point. This results in the point appearing as a blur, instead of a well-defined spot (Huang et al., 2009). Resolution is the smallest distance at which two objects that are close to one another can be distinguished. The limits of an observable resolution can be estimated according to Abbe's criterion from the following equation:

$$d = \frac{\lambda}{2NA},$$

Equation 1: Abbe's diffraction criterion of light. Source: (Abbe, 1873)

where d corresponds to the resolving distance, λ is the wavelength of the light in use and NA stands for the numerical aperture of the objective lens that collects the light (Abbe, 1873). High frequencies that are responsible for fine details are lost when a finite numeric aperture lens is used. The diffraction pattern of a single object is known as an Airy pattern, with the central diffraction spot as the 1st diffraction order, also known as Airy disk, and the subsequent rings referred to as 2nd order, and 3rd order. The Rayleigh criterion, derived from Abbe's criterion, states two entities are described as resolved when the first diffraction minimum of the first entity overlaps the maxima of the Airy disk of the second entity. The Rayleigh criterion, in the lateral dimensions, is defined by the following equation, which stems from Abbe's criterion:

$$d = \frac{1.22\lambda}{2NA},$$

Equation 2: Rayleigh's criterion for the resolution limit in lateral dimensions. Source: (Murphy, 2002) where d is the minimum resolved distance in the lateral dimensions, λ corresponds to the wavelength of the light source and NA corresponds to the numerical aperture of the objective lens in the microscopy system. The equation is dependent on the NA of the condenser and objective; if the condenser NA is less than the objective NA, their addition is taken into consideration (Murphy, 2002). The Rayleigh criterion is shown in Figure 1.

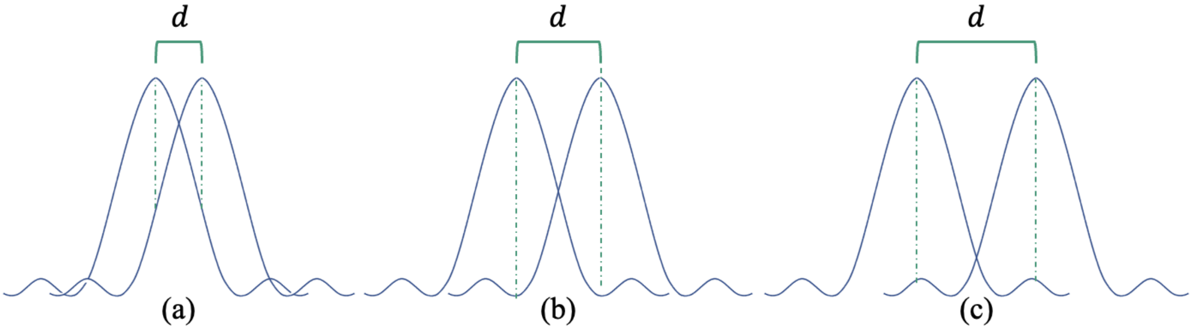

Figure 1: Rayleigh criterion, in lateral dimensions, in three scenarios where d is the resolving distance: (a) both objects are not resolved; (b) both objects are just resolved; (c) both objects are well resolved. In B, the central diffraction spot of the left object is coincident with the first minimum of the right object. Adapted from (Murphy, 2002).

A microscope image is the product of a convolution of the Point Spread Function (PSF) of the system and an imaged real complex object. The PSF is the response of the system to the point object emitter. The Airy pattern of an imaged object is also known as its PSF, although this equality depends on the presence of aberrations in the image. If there are no significant aberrations, the PSF is effectively the Airy disk of the object; on the contrary, the PSF will be considered broader and lacking in contrast (Young, 2003).

Ultimately, the resolving limit in microscopy is usually approximated to half the wavelength of the light in use, depending on the NA of the system. Thus, in practice, it is usually determined by the Full Width at Half Maxima (FWHM) of the PSF of a point. For instance, in a system where visible light (e.g. 550nm in wavelength) is used, the limit can be approximated to 200nm in the lateral axes, while the limit is usually twice or thrice in the Z axis, thus, around 500nm (Huang et al., 2009). The lateral resolution is inversely proportional to the NA of the objective in the first degree, as seen in Equation 2. Meanwhile, the axial resolution is inversely proportional to the square of the NA of the objective (Latychevskaia, 2019), as shown in **Equation 3**.

$$d = \frac{2\lambda}{(NA)^2},$$

Equation 3: Rayleigh criterion for axial resolution. Source: (Keller, 1995)

where d is the minimal resolved distance in Z, λ is the wavelength of the light in use and NA is the numerical aperture of the objective in the imaging system.

1.1.2. Optical Sectioning

In a traditional widefield microscope, the sample undergoes uniform illumination, which refers to illumination along the field of view of the objective. This results in the observation of several planes of the specimen at the same time, called uniform detection, preventing the emphasis of the focal plane. However, a concept called optical sectioning introduces the production of an image solely of the focal plane, removing out-of-focus light. The inclusion of a pinhole in the detection of the optical path is one major method to achieve optical sectioning, as it restricts the Airy disk of the imaged object, enabling to focus on intensities closer to the PSF maxima. The pinhole is adjusted in terms of Airy units, which refer to the diameter of the 1st diffraction order or Airy disk. Nevertheless, the implementation of structured illumination and structured detection by other means can also provide optical sectioning, since both processes are aimed at probing one specific area of the sample. Confocal microscopy, which features point illumination through laser as a light source and point detection through photosensitive detectors (charged-coupled devices, photomultipliers, photodiodes), provides optical sectioning albeit requiring scanning throughout the sample (Wilson, 2011).

As optical sectioning allows for the sample to be imaged solely at the focal plane, a series of sections are detected as the specimen is moved through the axial dimension. These stacks of images are computationally merged through image processing software to produce a three-dimensional reconstruction of the sample (Wilson, 2011). Additionally, computational processes, such as deconvolutions, can further improve optical sectioning by increasing contrast (Cai et al., 2018).

1.1.3. Signal-To-Noise Ratio and Contrast

Signal intensity with regards to the background is a major characteristic to analyze in imaging. The measured signal values are not a direct representation but a proportion of the number of photons emitted or scattered from the sample. Moreover, each measure of signal intensity is an approximation, and a variation is to be expected between repeated measurements. The proportion of acquired signal to the noise is inherently known as the Signal-to-Noise Ratio (SNR), where a high value leads to clearer signal. Still, noise is a vaguely defined characteristic, usually encompassing everything that alters a signal, for instance, resembling a "snowy output of a television receiver displaying the signal from a distant station" (Pawley, 2006). However, Pawley considers three main types for digitization of image data: Poisson noise (minimum uncertainty as a consequence of quantum mechanics), Readout noise (random variations in the electronics), and Quantum efficiency of the detector (linked to the increase of the effect of Poisson noise).

Contrast, another significant determinant in image production, refers to the difference between dark and light areas of an image (Cheng and Kriete, 1995). Contrast can be determined by the ratio of the change in image signal intensity and its average, and it is an essential component to image production similarly to the concept of resolution (Pawley, 2006).

1.1.4. Sampling rate

Another important aspect in the analysis of signals is the sample rate. Sampling refers to the conversion of a signal to a numeric sequence. The Nyquist theorem was based on the optimal strategy to digitally sample an analog signal, originally developed for telegraph signal analysis. Claude Shannon proved this theorem and elaborated further by showing the possibility to reconstruct an original signal from the digital values by properly measuring intensity values at intervals that are less than half the period of the highest frequency of the original signal. This is also known as the Shannon sampling frequency or the Nyquist frequency. In order to satisfy this condition in 2D images, the size of the pixels during the imaging detection process should be equal to the half of the Abbe criterion for resolution, knowing the diffraction limit established by Abbe is the maximum sharpness possible (Pawley, 2006). According to Pawley, in a current microscopical imaging, the smallest feature should be at least 4 pixels wide.

1.2. Physical Basis of Stimulated Emission Depletion Microscopy

The methods by which we observe a sample through a microscope have dramatically changed; from discerning the morphology of an entire sample by overall illumination, to resorting to complex chemical and physical procedures for imaging specific details of specimens or even cellular processes. This subchapter elaborates in the physical understanding of imaging techniques such as fluorescence and stimulated emission and their merging to obtain super resolution imaging.

1.2.1. Fluorescence

Fluorescence microscopy can be considered the biggest step forward in the development of cellular imaging, since it brought the possibility to target specific intracellular components with indicators. Still, this broad technique is bound by the physical limitations of light (Sanderson et al., 2014). Fluorescence is the process in which a molecule absorbs energy from a photon interaction to later emit some of this energy as a photon. Since energy is lost in the process, the emitted photon is of a longer wavelength than that of the initial photon interaction. The two energy exchange processes are known as excitation and emission, respectively, and can be depicted in the Jablonski diagram. The Jablonski diagram, illustrated in **Figure 2**, depicts the electronic states of the molecule and its energy transfer process. At the initial stage of the process, the molecule is set at its ground state, in a stable condition. As the incoming photon interacts with the molecule, the molecule absorbs the energy and its electrons are raised to a higher energy and vibrational singlet state, deemed as excited. This change of state of the molecule is called excitation. Within this singlet state, the electrons may go to its lowest vibrational level in the excited state losing energy through vibration and heat, until they emit photons and fall back to a higher vibrational level of the ground state (Schweizer et al., 2021). The collection of photons that excite the molecule are called the excitation light, and the photons emitted by the molecule as they reach their ground state are called the emission light. The difference between the intensity peaks of the excitation and emission spectra is called Stokes shift, after Sir George Gabriel Stokes (Lakowicz, 2006). Proper selection of the optical components is critical for ensuring fluorophore excitation, maximizing the SNR while minimizing background fluorescence, and limiting the damage to the ability of the molecules to emit light, also known as photobleaching and sample phototoxicity (Icha et al., 2017).

Despite the general understanding of fluorescence occurring in a single photon excitation and emission process, it is also possible for a molecule to interact with multiple photons yet emit only one photon. It is worth noting the energy of each emitted photon is still less than the energy of the absorbed photons. This phenomenon is called two-photon, or multi-photon, microscopy. However, this process may only develop with a high spatial and temporal density of photons due to the required simultaneous encounter with the molecule; a situation in which specialized, high-powered light sources would be needed (Sanderson et al., 2014).

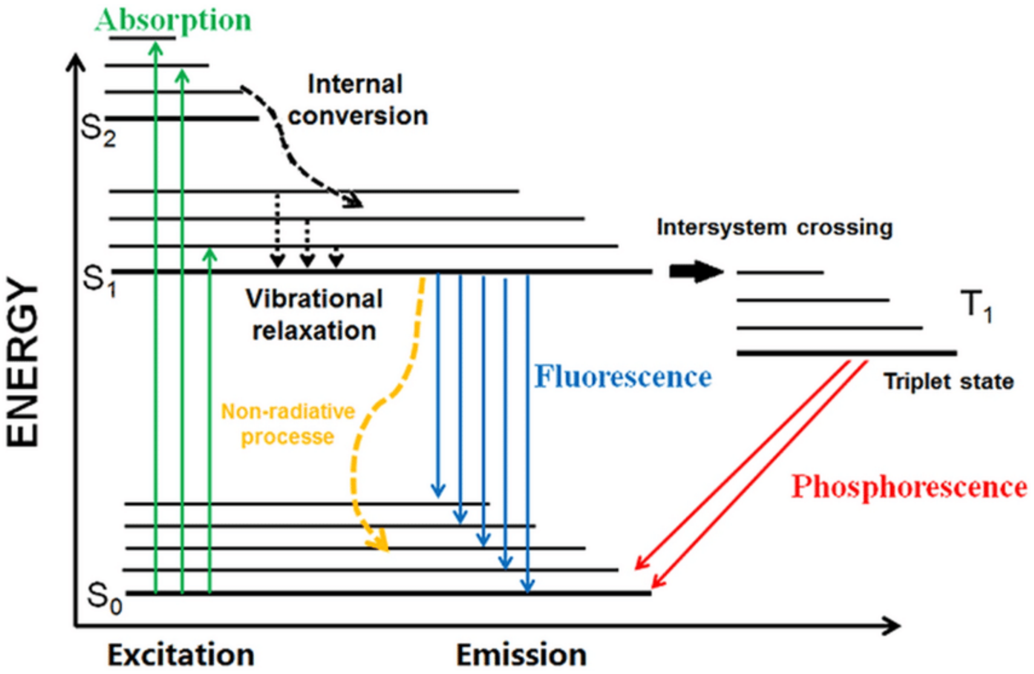

Figure 2: Jablonski diagram depicting the processes of fluorescence, internal conversions, and intersystem crossing towards a triplet state that leads to phosphorescence. The line colors do not reflect wavelength spectra. Source: (Schweizer et al., 2021)

1.2.1. Spontaneous and Stimulated Emission

The random emission of photons by the excited molecule is known as spontaneous emission, although it is properly described as the process of the quantum jump from a molecule as it transitions from an excited state to a lower singlet state (Hoang et al., 2015)**.** Furthermore, there is an alternative emission procedure known as stimulated emission (SE). The process of stimulated emission occurs when an excited molecule collides with a photon of a similar energy to that of the difference between the excited state and ground state, forcing the molecule to emit light of a similar energy as the incoming photon, instead of the expected emission spectra, as the state of the molecule returns to its ground level (Huang et al., 2009). The principles of spontaneous and stimulated emission are shown in **Figure 3**.

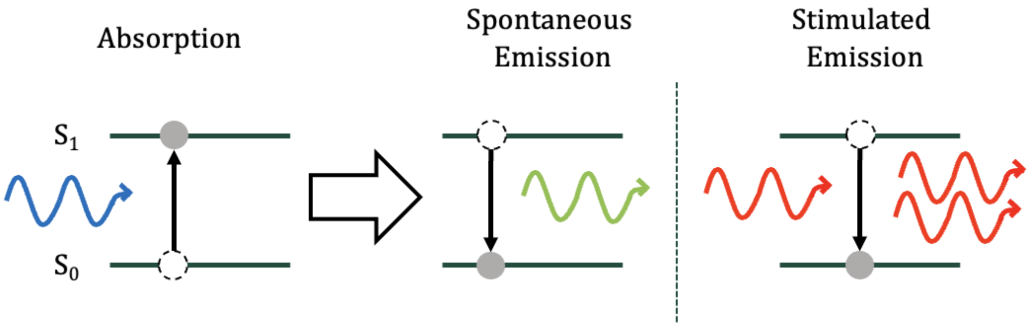

Figure 3: An excited fluorophore (left) can lead to emission by spontaneous means (middle) or can be induced to emit light by an external agent (right). The spontaneous process leads to

emission of light with its expected wavelength, whereas the stimulated process is often used to produce an emission of light of a similar wavelength as the stimulation.

1.2.2. Stimulated Emission Depletion Microscopy Principle

Imaging techniques to effectively bypass the diffraction limit of light have been developed since the 1990s. They are collectively referred to as super-resolution techniques, and the number of available approaches has grown considerably since its inception (Jacquemet et al., 2020).

One of the earliest super resolution techniques is Stimulated Emission Depletion (STED) Microscopy, developed theoretically by Stefan Hell in 1994, and experimentally in 2000. Later in 2014, he was jointly awarded the Nobel Prize for Chemistry for his work in fluorescence super-resolution microscopy, along with two other researchers. One of the other recipients, W. E. Moerner, developed an approach to bypass the diffraction limit of light and detect single molecules and their precise location at the nanoscale (Möckl et al., 2014), from which the third recipient, Eric Betzig, developed a fluorescence technique by selectively imaging several excited fluorescent proteins, positioned at distances just above the diffraction limit, until the proteins bleached. Then, additional proteins would be excited and imaged until bleaching, and their images would be processed using probability theory to sharpen them. From superimposing all obtained images, a super-resolved image would be produced (Betzig et al., 2006).

As the name of the imaging technique implies, it employs the concept of stimulated emission in an additional laser beam, called the depletion beam, to control the emission spectra of particularly located excited fluorophores, while allowing others to naturally fluoresce. Scanning throughout the sample following the principle would produce a sub-diffraction resolution image. The stimulated emission is most effective when the depletion beam is concentrated in a timeframe shortly after the fluorophore excitation yet no longer than the fluorescence lifetime. Otherwise, there is a possibility for a grounded fluorophore to be re-excited by the stimulated emission due to the previously mentioned difference in energy (Gould et al., 2017). **Figure 4** shows the representation of the principle of STED microscopy.

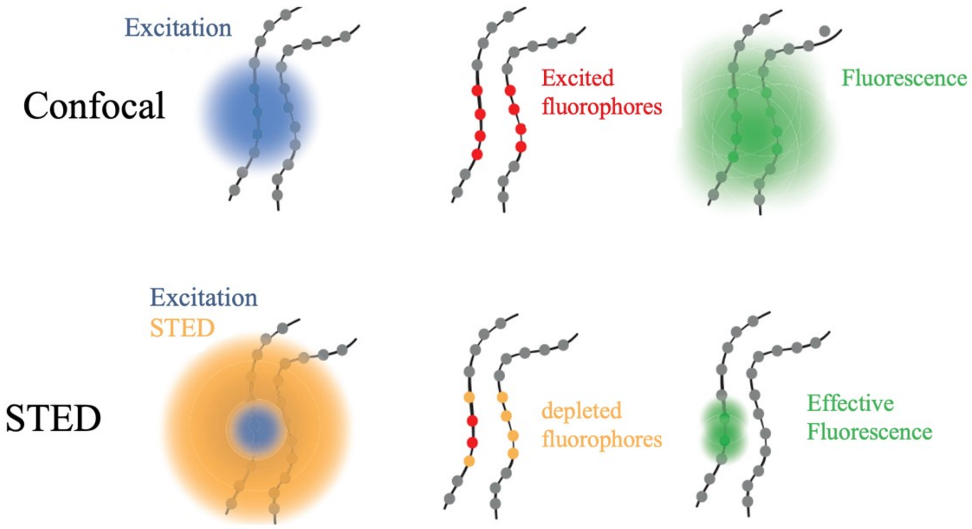

Figure 4: STED principle over filament-like sample. (above) In Confocal microscopy, the excitation laser (blue) excites the fluorophores in a diffraction-limited region, leading to emission of a wide area losing details of the sample; (below) in STED microscopy, the excitation and STED lasers jointly illuminate the sample, where the excitation laser is only present at the central intensity-zero region of the depletion laser, allowing the fluorophores solely within this region to fluoresce. Source: (Dijkstra, 2012)

From Abbe’s criterion regarding the diffraction of light, Hell was able to append elements to the original equation:

$$d = \frac{\lambda}{2NA * \sqrt{1 + \frac{I}{I_s}}},$$

Equation 4: Abbe's diffraction limit with appended elements for super-resolution technique STED. Source:(Blom and Brismar, 2014)

where I refers to the applied maximum intensity of the STED beam and I_s is the intensity at which a portion corresponding to 1/e of the molecules are depleted by the STED beam (Wildanger et al., 2009). **Figure 5** presents the effect of the depletion beam power over the resulting observable sub-diffraction regions of interest.

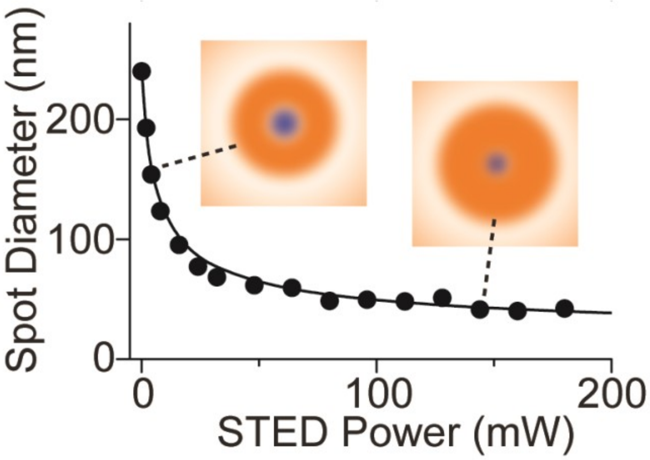

Figure 5: Graph representing the relation between spot diameter in nanometers and the STED beam power in milliwatts. The resulting emission area (dark blue) decreases as the intensity of the depletion beam (orange) increases. To be noticed in this scenario, after 50mW there is no significant decrease in spot diameter, thus high depletion power may not ensure unlimited resolving power. Source: (Clausen et al., 2014)

1.3. STED Instrumentation

The following subchapter extends on the optical components and characteristics required to design a Stimulated Emission Depletion microscope, including light sources, detectors, fluorophore and filter selection, and the modulation of the depletion beam.

1.3.1. STED implementation over Confocal Microscopy structure

In modern fluorescence imaging, higher specificity is achieved by applying limits to the background fluorescence emanating from the emitted illumination from the sample in an optical configuration called confocal microscopy. This imaging device illuminates the sample one single point at a time, excluding any scattered light that may obscure the resulting image. The widely accepted choice of light source is the laser, which inherently encompasses a wide collection of specific wavelengths to work with as their intensity maximas can be constricted within short wavelength ranges. This optical configuration also employs a pinhole positioned before the detector in the optical path. The combination of point illumination and point detection allows the processing of light only from the focal plane of the sample. Moreover, it provides a better contrast and less haze than conventional microscopy could (Semwogerere and Weeks, 2008). However, while the resolution is considerably enhanced, this improvement does not truly augment the resolving power of the microscope, but reduces the out-of-focus light as previously mentioned. The optical configuration of STED microscopy is adapted from the confocal microscopy, expanding it by the addition of a secondary laser which provokes the stimulate emission on the fluorophores adjacent to the area of interest. **Figure 6** depicts a simplified representation of a STED microscope and the effect of the depletion beam on the fluorescent area of interest.

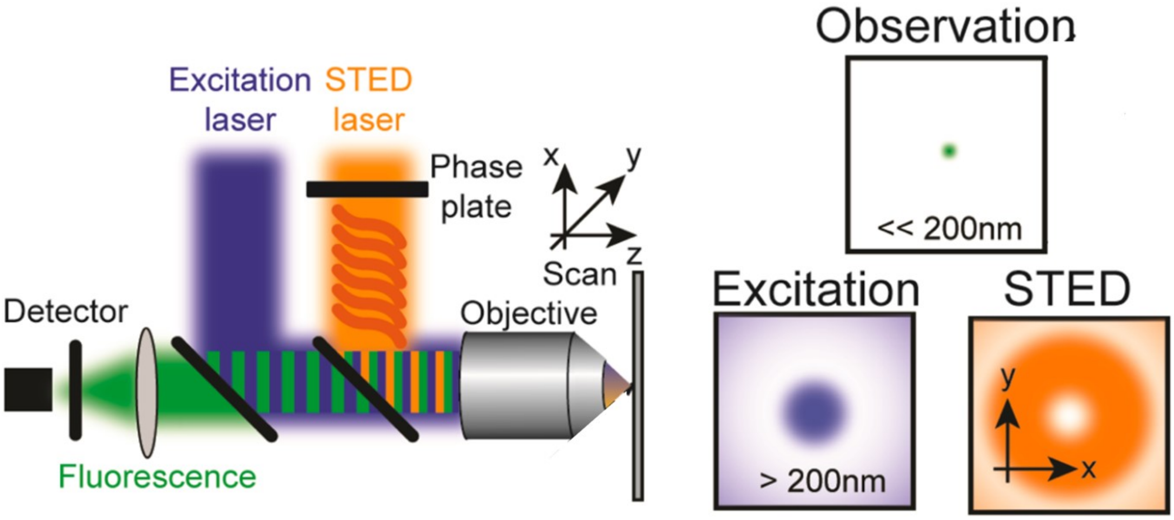

Figure 6: (left) Representation of the STED microscopy, where the excitation laser (dark blue) and the STED laser (orange) are joined and focused on the sample at the right, and the resulting emission light (green) is collected by the detector; (right) The excitation laser follows a diffraction-limited Gaussian focus, whereas the STED laser is modulated by a phase plate which alters the behavior from Gaussian to an intensity distribution with a central intensity-zero. When the excitation and STED lasers are joined, either coherently or incoherently, the resulting observational section is smaller than the diffraction limit. Source: (Clausen et al., 2014)

1.3.2. Light sources in STED microscopy

Since its conception, the source for the excitation and depletion light in STED microscopy has been established as a laser, due to its inherent point-source nature (Hell and Wichmann, 1994). The process of stimulated emission serves as the basis for lasers as a light source, as its acronym describes, Light Amplification by Stimulated Emission of Radiation. In 1916, Albert Einstein suggested the release of excess energy as light by atoms in his paper "On the Quantum Theory of Radiation", providing the theoretical foundation for stimulated emission (Einstein, 1916). Considering a chamber consisting of two opposing mirrors and active laser material, before the process starts, excited atoms within the chamber will emit light by spontaneous emission. Only those atoms whose emitted light is oriented towards the axis, or close, will stay long enough within the cavity to undergo enhancement by stimulated emission (Haken, 1970).

The excitation laser wavelength is dependent on the characteristics of the fluorophores to be imaged. For example, according to Wurm et al., (2012), rhodamine dyes present good photophysical properties, citing Atto647N as one of the most frequently used dyes for single molecule, confocal and STED microscopy. This fluorophore could be excited with 620-650nm. However, the depletion beam is expected to entirely promote stimulated emission and not be absorbed. Following the example, a depletion beam could be set at 750-775nm, being positioned at the far end of the emission spectra of the fluorophore, ensuring not to interfere with the emission detection. Figure 7 depicts the excitation and emission spectra from Atto647N 2, as well as the excitation and depletion beams.

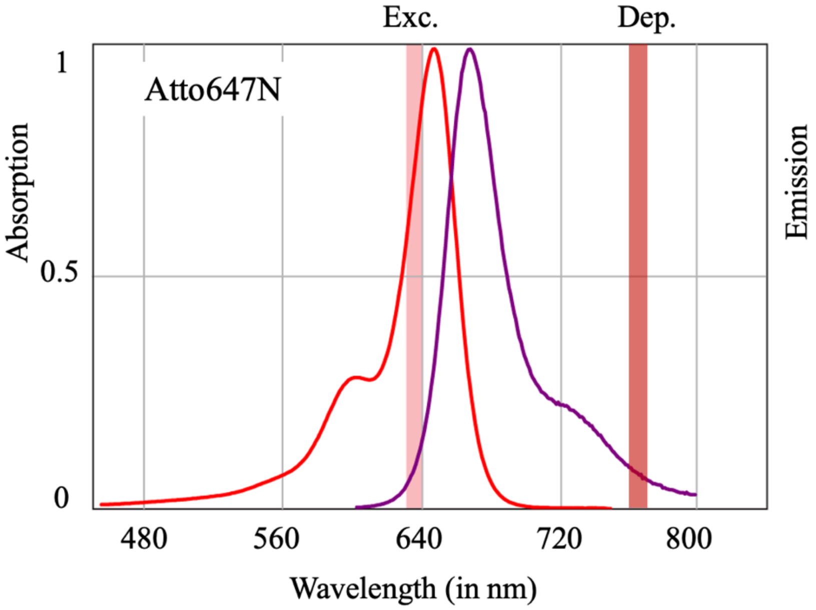

Figure 7: Absorption and emission spectra form Atto647N, where the wavelength of the excitation laser is approaching the excitation maxima of the absorption spectrum, and the depletion laser at the far end of the emission spectrum. Source: Adapted from (Wurm et al., 2012)

There are two main types of laser work regimes, pulsed and continuous wave (CW). Pulsed laser is performed with high intensity pulses of energy, averaging to a lower peak, where the excitation beam is synchronized with the depletion beam so as the latter follows the former simultaneously within the timeframe of the fluorescent state (Donnert et al., 2006). Further, pulsed lasers allow for time-delay between excitation and depletion, optimizing the stimulated emission process (Farahani et al., 2010). Pulsed laser is the earliest configuration for STED and produces the best images according to Wu et al. Nevertheless, high power laser for depletion can be expensive (Wu et al., 2016). Continuous wave laser works by providing a continuous stream of energy, averaging at its peak. CW does not implicate the complex time synchronization between excitation and depletion and a laser source with similar optical power between the main types is more affordable when choosing the CW configuration (Wu et al., 2016). The level of sophistication of the configuration for pulsed laser hindered the choice of researchers to use it as light source for STED imaging. Thus, Willig et al. adapted and analyzed CW in STED imaging, although comparing the laser source to the confocal imaging limitations, showing a low peak intensity required, 5-8 fold in lateral and 3.5 fold in axial improvement in resolution compared to diffraction limited confocal, and reducing unwanted multiphoton excitation of fluorophores. However, CW is not able to produce comparable resolutions to pulsed laser STED configurations without an increase in average depletion power (Willig et al., 2007). A promising yet complicated technique to improve the resolution is to sweep the CW laser beams throughout the sample at a speed high enough for few successive pulses to be able to strike the same fluorophore, though several scans are required for enough signal accumulation (Gould et al., 2017). Vicidomini et al. mentioned the implementation of CW lasers comes with reductions in the Signal-to-Noise Ratio (SNR), despite its simplicity and low cost in implementation (Vicidomini et al., 2018). Moreover, time gating can be implemented for both types of lasers in a concept known as gated-STED, where the fluorescence detection is performed in a specific interval of time, resulting in a considerable decrease of the fluorescence signal which creates the STED images. Furthermore, this signal reduction improves the depletion effect with no substantial increase in the depletion beam intensity (Vicidomini et al., 2018).

1.3.3. Fluorophore selection, special photostable dyes

At its inception, STED had a limited range of dyes, due to its need for photostability and brightness. Rhodamine B was named as a potential dye in the original proposal (Hell and Wichmann, 1994). In later publications typical laser dyes whose emission range was near the red spectrum, such as Pyridine 2 and 4 were used (Klar and Hell, 1999). However, by the beginning of the last decade, more than 40 fluorophores across the visible spectrum had been subject to STED imaging. Immunolabeling is the recent gold-standard for STED imaging, allowing for the labeling of structures in fixed and permeabilized cells and for the expression of components located at the surface of living cells. Nevertheless, most STED imaging research is focused on structural analyses, where the use of one dye is sufficient. An additional, separate channel is necessary for studying processes such as protein interactions and structural or functional dependencies (Müller et al., 2012). Advances in STED imaging have led to multicolor imaging, where traditionally a dedicated configuration of beams for excitation and depletion for two or more fluorescent dyes were developed, albeit at high cost and complexity. Alternatively, a reduction of cost and complexity was reached by using two fluorophores with slight overlapping emission spectra and a wide Stokes redshift while using only one depletion beam with two excitation laser beams. Moreover, the use of a supercontinuum pulser laser as light source, with an adjustable output wavelength between 400 and 2400nm which was also the source for depletion beam at low power, enabled two-color STED imaging combined with digital enhancement for mitochondria and microtubules in live cells (Zhang et al., 2021). Table 1 enumerates some of Abberior made dyes for STED imaging.

Table 1: Abberior Fluorophores used in STED imaging research.

Fluorophore	**Absorption Max (in nm)**	**Emission Max (in nm)**	**STED Wavelength (in nm)**	**Reference**
Abberior STAR 440	432	511	590-610	(Gemmink, 2017)
Abberior STAR GREEN	493	519	590-610	(Yan et al., 2022)
Abberior STAR ORANGE	589	616	750-800	
Abberior STAR 512	511	530	590-610	(Likhotkin et al., 2023) Used in Multicolor setup
Abberior STAR 580	587	607	750-800	(Mol and Vlijm, 2022) Used in Multicolor setup
Abberior STAR 635	635	655	750-800	
Abberior Live 510	498	529	590-610	(Grimm et al., 2019)
Abberior Live 515	515	541	590-610	
Abberior Live 550	551	573	650-775	(Gregor et al., 2022) Used in Two color setup
Abberior Live 610	611	636	750-800	
Abberior Cage 552	552	574	650-775	(Reuss et al., 2017)

1.3.4. Filter set

In fluorescence imaging, filters are used to select specific wavelengths throughout the light path. Filter sets are constructed depending on the excitation and emission spectra of any specific dye (Lakowicz, 2006). Filters are commonly divided into three categories: excitation filters, emission filters and dichromatic beamsplitters or dichroic mirrors. Excitation filters allow the transmission of specific wavelengths through them originating from the light source towards the sample. Emission filters are similar to excitation filters; however, they are positioned to absorb excitation light within the system and allow only light from emission to go through, towards the detector. Finally, the dichroic mirror reflects one or several spectra while transmits others. Dichroic mirrors reflect the excitation light in direction to the sample, and transmit the emission light towards the emission filter, and to the detector (Herman, 1998). Figure 8 shows a simplified view of a filter set within a cube.

Filters are also divided into short pass, bandpass and long pass. Short pass filters allow a range of short wavelengths, before displaying a steep drop when reaching the limit wavelength. Long pass filters display the opposite behavior to short pass, with the steep rise at a certain wavelength, allowing for a range of longer wavelengths to pass. Bandpass filters exhibit the behavior of a combination of long and short pass filters. While the previous filters block light of the wavelengths outside their limit, dichroic mirrors reflect certain wavelength range and transmit the remaining range (Herman, 1998). The combination of filters must be accurate with the fluorophores spectra to ensure the excitation and emission peaks are observed. Overlaps from both excitation and emission spectra are also possible and may result in unwanted fluorescence background when not properly addressed (Lakowicz, 2006). In STED imaging, the spectrum of the depletion beam must be positioned at the far end of the emission spectrum tail avoiding any overlapping with the excitation spectrum to prevent re-absorption, and further, avoiding the depletion of the emission spectrum peak (Farahani et al., 2010).

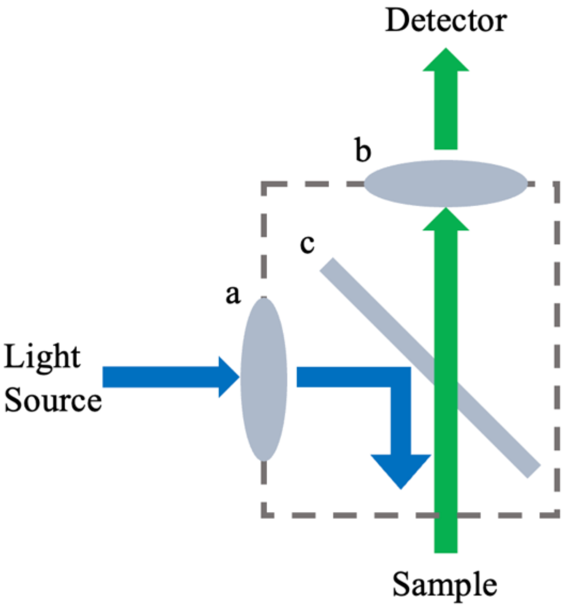

Figure 8: Simplified filter set within cube, where (a) corresponds to the excitation filter, (b) corresponds to the emission filter, and (c) is the dichroic mirror. The blue arrows represent the excitation light, while the green arrows show the emission light.

Some filter sets used in STED imaging include, but are not limited to, GFP (469-35 for excitation, 525-39 for emission, and 497 for dichroic mirror), Cy3 (531-40 for excitation, 593-40 for emission, and 562 for dichroic mirror), and Cy5 (628-40 for excitation, 692-40 for emission, and 660 for dichroic mirror). Common configurations depict two dichroic mirrors, one for the excitation beam and another for the depletion beam, in addition to the emission filter, as seen in different STED layouts.

1.3.5. Detectors and Gated STED

Since its inception, STED has been executed with its detection as a single-photon process (Klar and Hell, 1999). Light is composed of photons essentially, and single-photon detectors are devices sensitive enough to detect single-photon clicks (Liang and Zeng, 2014). Avalanche photodiodes (APDs), usually InGaAs/InP, are highly efficient in detecting near-infrared photons. However, avalanche signals from weak photons tend to be buried in spike noise due to charging and discharging from the APD capacitance required by the gating pulse (Liang et al., 2011). The main operation of the APDs is by active-quenching, which refers to the quenching the APD by a reduction of the voltage build-up after a photon detection on the APD. A "dead time" follows which corresponds to the time the APD takes to recover for the next photon detection. Further, APDs are able to work in room temperatures, or slightly below, unlike superconducting nanowire single-photon detectors which require cryogenic temperatures (Wu et al., 2023).

In order to ensure proper beam alignment, the photomultiplier tube (PMT) is used as the detector in reflection mode scans as it allows for direct visualization of the STED beam profile (Barbotin, 2020). The PMT contains a photocathode, as the ADP, numerous dynodes, and an anode in a sealed glass envelope with a high vacuum inside. The process undergoes as follows: as photons enter the tube, they excite electrons called photoelectrons. These photoelectrons are then focused onto the first dynode, which is a secondary-electron emission surface, where they are multiplied through the dynode effect, repeatedly on each dynode of the device, obtaining high-gain amplification. Lastly, secondary electrons are collected near the last dynode in the anode, and a current spike is detected by the corresponding electronic device (Polyakov, 2013).

A significant improvement in signal detection in STED microscopy is the development of Gated STED (g-STED), a technique which analyzes the fluorescent behavior in time to improve the effective spatial resolution (Vicidomini and Moneron, 2013). This technique was proposed on a STED microscope setup where the excitation laser was pulsed, and the depletion laser was continuous wave (CW). The advantage of CW is the lower power intensity for the depletion beam, albeit with a lower resolution. However, the conjunction with timed gating is sufficient enough to produce details that on CW alone would be lost.

The combination of the excitation and depletion beams is developed during the excitation pulse, around less than 150ps. Nonetheless, the depletion beam is maintained to promote the possibility of full depletion of the surrounding fluorophores. Vicidomini et al. suggest the resolution is as dependent on the intensity of the depletion beam as on the duration of the depletion beam action. The effective fluorescence lifetime of a fluorophore is mainly influenced by the presence of the depletion beam. While the fluorophore is near the maximum intensity of the depletion beam, near the crest of the central zero intensity area, the fluorescence lifetime is at its minimum. This relationship can be used to reject the emission from depleted fluorophores and accept that of the long-lived fluorophores within the central zero-intensity area. Thus, detecting photons after a delay improves the fluorescence on-off contrast that produces the sub-diffraction resolution, and guarantees the fluorescence is collected mainly from the central area of the depletion beam (Vicidomini et al., 2011).

1.3.6. Phase modulation

The depletion beam in STED microscopy is modified by altering its phase, traditionally using a physical vortex plate. Most recently, the implementation of Spatial Light Modulators (SLMs) allows for a more flexible configuration (Harke et al., 2013). The vortex plate adds angular momentum around the optical axis of the laser beam, and while preserving its rotational symmetry, the beam becomes hollow. The same handedness as the angular momentum must be maintained when circularly polarizing the depletion beam to ensure the central zero-intensity is a true zero (Wu et al., 2016). Additionally, vortex plates feature several standard and segmented physical waveplates which enable the use of large spectral bandwidths, allowing for multicolor STED using one depletion beam with several excitation beams (Reuss et al., 2010).

The Spatial Light Modulator is an adaptive optics device that contains liquid crystal pixels in a two-dimensional array with which the amplitude and or phase of a laser beam can be modulated by reflection (Liquid Crystal Technology on Silicon - LCOS) or transmission (Liquid Crystal Display - LCD) (Frumker and Silberberg, 2007). A relation between gray values from a digital image and electrical voltages is established. The voltages produce a tilt on the pixels of the liquid crystal, changing the refractive index of the liquid crystal. Thus, the laser beam is altered after its reflection on the SLM. This device is also capable of providing corrections to optical defects, e.g., aberrations, and beam auto-alignment (Vicidomini et al., 2018) which proves advantageous over vortex plates.

Depending on the sought effect, both beam modulating devices often require quarter or half waveplates to ensure polarization alignment is maintained (Moreno et al., 2012).

1.4. Special considerations in STED Microscopy

As in any imaging technique, there are certain considerations that require attention when imaging following the principles of Stimulated Emission Depletion microscopy.

1.4.1. Photobleaching

One significant consequence of the depletion beam is the high possibility to photobleach the samples, or nullify the fluorophore ability to fluoresce. Fluorophores have a probability to cause irreversible covalent modifications once they interact with other molecules during their excitation state (Vicidomini et al., 2018). Beside fluorophore re-excitation, the depletion beam can also incite the fluorophore to higher electronic states where the probability of photobleaching is higher (Hotta et al., 2010).

Nevertheless, different approaches have been considered to reduce photobleaching. For instance, one approach is to lessen the fluorophore illumination while on the triplet state, as Donnert et al., (2006) show in their work with the use of low-repetition-rate pulsed lasers enabling the removal of any dark states that exist in the intervals between the pulses. Furthermore, Staudt et al., (2011) propose reducing useless illumination by focusing the excitation and depletion beams only on pixels related with sub-diffraction regions, preventing unrequired state transition cycles on further fluorophores, following the RESCue approach, for lessening photobleaching. Chemical changes in the embedding medium composition can also diminish photobleaching, although they may prove incompatible with live-cell experiments (Beater et al., 2014).

1.4.2. APD detection speed

As previously mentioned, APDs are used as the main detecting device in STED imaging. APDs are usually gated on MHz frequencies, with their active gate lasting nanoseconds. This is to eliminate the probability of afterpulses, which are false inductions of photon detection due to impurities and lattice defects in the APDs, which can lead to miscounts (Krainak, 2005). Further, due to their principles of operation, there is a time delay of microseconds (Yuan et al.,

2007) , known as dead time, after a photon detection in which the detector and other electronic components cannot register further photons. This is to prevent an effect called pile-up, an over-representation of early photos in a resulting analysis; the first photon would be registered by the system but subsequent photons would be lost (Wahl, 2014).

Moreover, from the Nyquist's sampling theorem, for a realizable high lateral resolution, for instance of 50nm, the theorem requires a pixel size as low as 20nm. This implies increased acquisition times and propensity to damage of the sample by photobleaching (Lenz and Tønnesen, 2019).

1.4.3. Aberrations

The excitation and depletion beam can be subject to common aberrations, for instance astigmatism, coma, trefoil, and spherical aberration. Li et al. go into detail about the different aspects in which each aberration previously mentioned affect both the depletion beam and the resulting effective PSF. They conclude spherical aberrations are the least affectual when analyzing the PSF, while astigmatism stretches the shape and considerably reduces the peak intensity of the PSF. They continue on to suggest a "positive relationship" between the aberrations and the depletion beam power intensity; sensitivity to aberrations on the PSF increases when reaching for higher resolutions (Li et al., 2018). Nevertheless, the Spatial Light Modulator is capable of effectively excluding aberrations from the depletion beam at the moment of modulation (Vicidomini et al., 2018).

1.5. Implementations of STED

Over the past three decades, researchers have expanded the Stimulated Emission Depletion microscopy technique by introducing new technologies and methods to improve results.

1.5.1. Adaptive optics

Adaptive optics (AO) are optical components that can be deformed to restitute incoming light waves, generally by use of deformable mirrors. Barbotin et al. implemented these components in STED microscopy, mostly confined to the axial dimension. Through the use of adaptive optics, they were able to correct residual system aberrations, as well as effects on spatial drift, laser misalignments on behalf of chromatic aberration, and especially, aberrations from refractive index mismatch, avoiding the need to change objectives, or other manual readjustments. **Figure 9** shows possible alterations on the depletion beam modulation from the adaptive optics component within the used optical path (Barbotin et al., 2019).

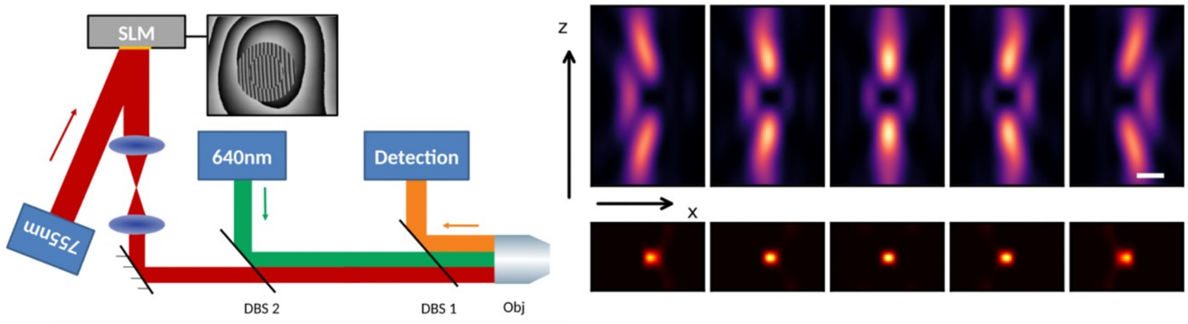

Figure 9: Alterations leading to aberration corrections in the depletion beam from adaptive optics component, SLM. (left) Optical setup used; (right) effects of the depletion beam alterations to the resulting resolution of the imaging system. Scale: 400nm. Source: (Barbotin et al., 2019)

Gould et al. implemented adaptive optics for 3D imaging using STED microscopy to observe its effects on thick biological tissues, which prompt strongly aberrated imaging conditions. They were able to correct the aberrations by a process of image optimization using a sensorless AO scheme. Further, a central λ/2 phase mask for improving 3D resolution was added to the imaging setup. The authors claim their scheme enables aberration correction using the super-resolution image, which may promote the use of automated AO as a functioning strategy for biological super-resolution. **Figure 10** shows the optical path through which Gould et al. developed their research, as well as the results from the aberration correction. (Gould et al., 2012).

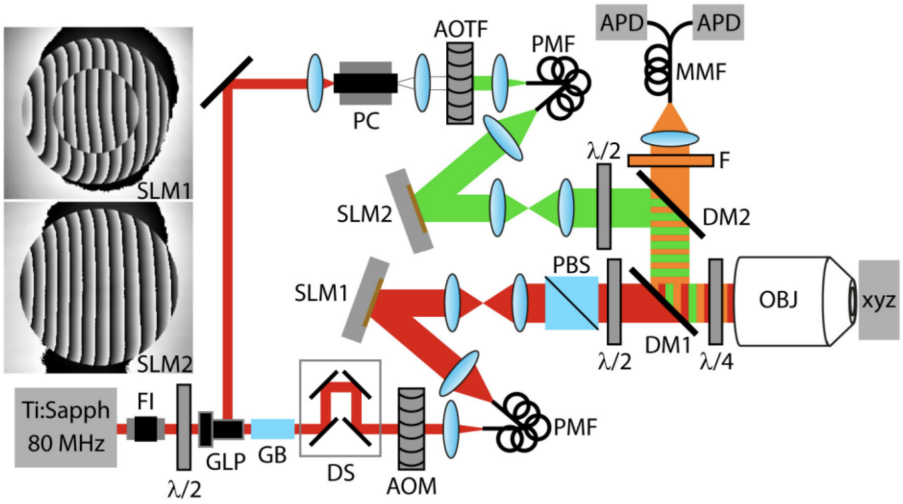

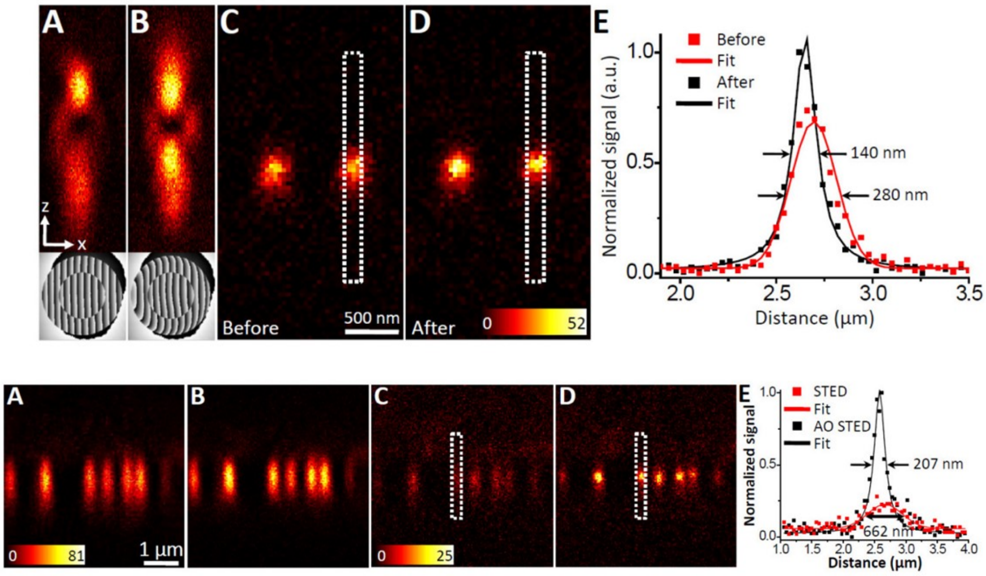

Figure 10: (above) Optical setup with 2 SLMs for aberration correction purposes. Abbreviations are as follows: FI – Faraday Isolator, GLP – Glan laser polarizer, GB- glass block, DS – delay stage, AOM – acousto-optical modulator, PMF – polarization-maintaining fiber, SLM 1 and 2 – Spatial Light Modulators, PC – photonic crystal fiber, AOTF – acousto-optical tunable fiber, PBS – polarizing beam splitter cube, λ/2 – half-wave plate, λ/4 – quarter wave plate, DM 1 and 2 – dichroic mirrors, F – bandpass filter, MMD – multimode fiber, APD – avalanche photodiode, OBJ – objective lens, xyz – piezo sample stage with 3 axes. SLM1 and SLM2 at the side depicts their respective phase patterns, which include baseline flatness corrections for the SLM, and a circular blazed grating. (middle) Correction of residual system aberrations. (a, b) STED PSF before and after corrections for system induced aberrations, (c, d) xz STED images before and after correction system induced aberrations of 100nm fluorescent beads, (e) axial line profiles of the pixels from the dotted boxes in (c, d). (below) Resulting images of 100nm fluorescent beads. (a,b) Beads at xz plane, in confocal mode before and after correction of sample induced aberrations. (c) STED mode with correction to the excitation beam, and (d) corrections to the excitation and depletion beam paths. (e) Axial profiles of the pixels from the dotted lines in (c, d) which show improvement in resolution and signal after aberration correction. Source: (Gould et al., 2012)

1.5.2. Two-photon excitation in STED

Two-photon excitation (2PE) is another alternative setup for STED microscopy which involves a major modification to the excitation process of the fluorophores. The traditional way of exciting a fluorophore requires one photon to inject the sufficient energy for the electrons of said fluorophore to jump to the excited state. However, Göppert-Mayer (1931) proposed a theory for two-photon quantum transitions in atoms and molecules, which is the basis for 2PE: excitation by two simultaneous photons that jointly provide the energy as one photon would require. Figure 11 shows the comparison of traditional excitation (also known as 1PE), 2PE and even 3PE, with the corresponding spontaneous emission. Additionally, while 1PE usually requires light sources from the short wavelength range of the radiation spectrum, 2PE can occur with sources of the long wavelength range, in the near infrared region of the spectrum.

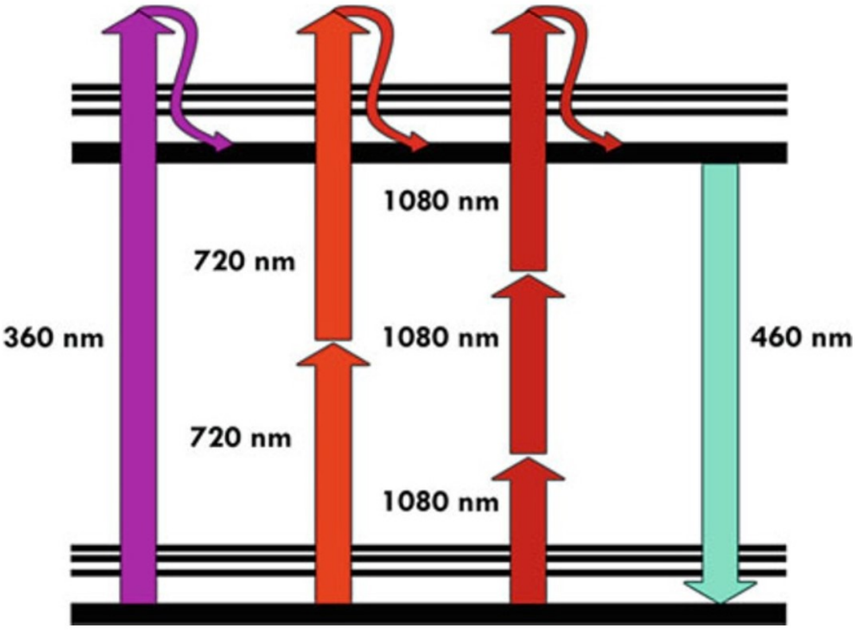

Figure 11: Simplified Perrin-Jablonski diagram depicting one-photon (1PE), two-photon (2PE), and three-photon (3PE) excitation. The emission process remains the same for all. Note the increasing wavelengths of 2PE and 3PE to maintain the sufficient energy as 1PE. Source: (Diaspro et al., 2006)

In 2PE, the excitation inducing energy, which requires at least two photons at each interaction, depends on the square power of the instantaneous intensity. Moreover, while the excitation power of traditional excitation is reduced as the square of the distance from the focal point of the lens, the reduction is reduced by the fourth power for 2PE. Thus, the fluorophores not positioned at the focal area will undergo excitation. This results in a pinhole effect as in confocal imaging without requiring a physical pinhole (Harke et al., 2013).

The benefits of 2PE for the excitation process are fivefold: the reduction of photo-interactions due to the low probability to induce excitation on fluorophores adjacent to the focal area, leading to the possibility for imaging living specimens over extended periods; the ability to perform with high sensitivity in a background free environment, derived from the filtering effect alike to a pinhole; the augmentation of depth for sample imaging (from few hundred µm to 1mm) since the light source can be of the long wavelength range; the reduction of colocalization errors; and the ability to prime photochemical reactions in under femtoliter volumes within cells and tissues (Diaspro and Bianchini, 2013).

1.5.3. Image Scanning Microscopy in STED

The original development of STED involved a single-photon detection system, an avalanche photodiode, collecting single items of information at a time (Klar and Hell, 1999). Nevertheless, single-photon detection has its drawbacks as previously mentioned. Tortarolo et al. developed a STED setup in which a detector array was used, enabling image scanning microscopy (ISM), shown in **Figure 12**.

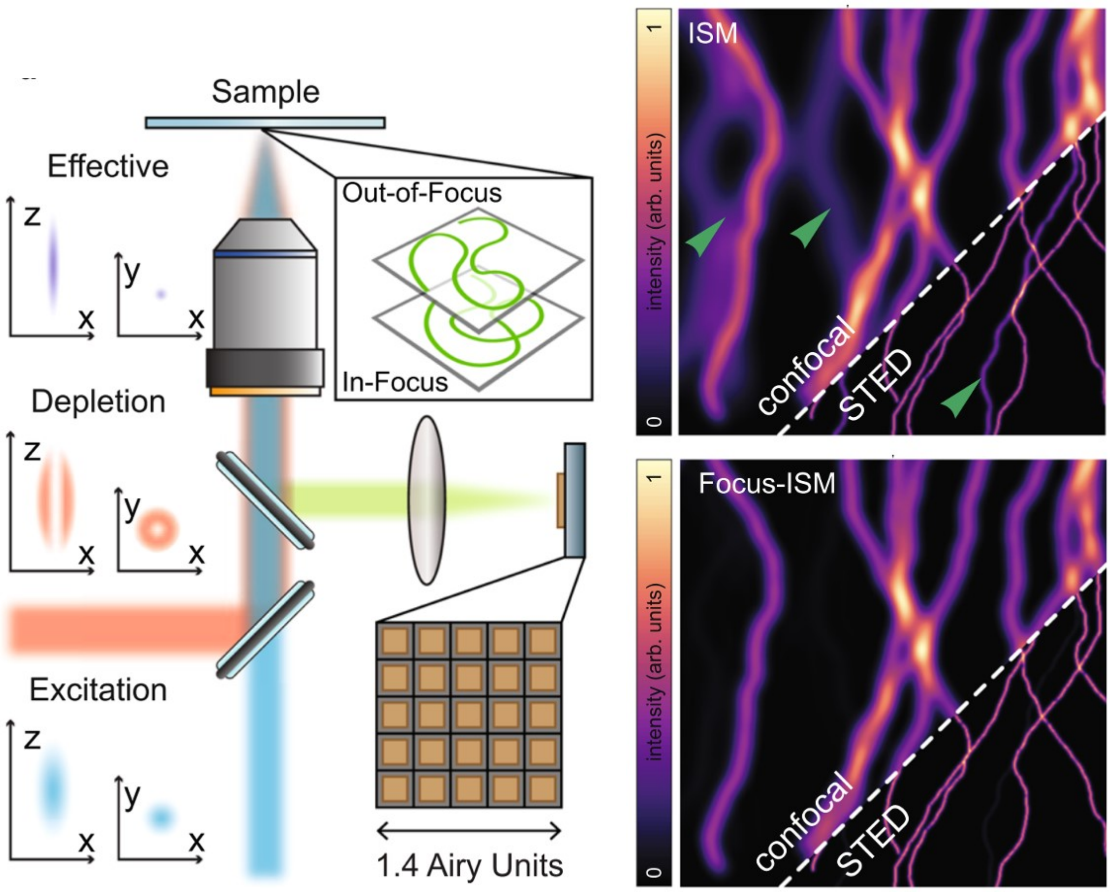

Figure 12: (left) Optical setup for ISM-STED microscope with a 5x5 detector array. (right) Comparison of confocal and STED imaging where the Adaptive Pixel Reassignment concept of Image Scanning microscopy is applied. In the lower result, Focus-ISM is shown, an algorithm developed by the authors were the photons of each post-algorithm micro-image (image obtained by the detector array) is classified as background or signal, before producing the resulting high resolution image. Source: (Tortarolo et al., 2022)

This imaging technique allows for obtaining small wide-field images of the central zero-intensity region, often referred to as micro-images, which contain axial and lateral information of the sample for later reconstruction to produce a super-resolved image. A commonly used algorithm is the Pixel Reassignment concept, where the signal detected by a pixel is reassigned to the most likely area (Singh et al., 2021). Through this expansion in detection, a reduction of the depletion beam intensity was possible whilst achieving a higher resolution, and suppression of out-of-focus background, compared to STED microscopy. However, this latter achievement is mostly done with a second implementation, a classification algorithm run after the signal acquisition for improved focusing. The authors claim their strategy requires minimal changes to the conventional microscopy setup, whilst presents significant advantages when imaging live and thick specimens (Tortarolo et al., 2022).

1.6. Types of STED masks

The modulation of the phase of the depletion beam is one, if not the most, important aspect of STED microscopy, as it dictates which fluorophores will be allowed to naturally fluoresce to produce the super-resolved image. Different configurations of the phase mask exist, yet two remain the optimum choice for either lateral, or axial restriction.

1.6.1. 2D-STED and z-STED

The depletion beam requires a specific shape to enhance the final resolution. The geometry sought after is that of a central zero-intensity area. Keller et al., (2007) developed a method to effectively search for zero intensity point patterns on a RESOLFT microscopy setup and concluded on two phase mask patterns, one of which provides optimum confinement in lateral dimensions and the other in the axial dimension. The former, commonly referred to as 2D-STED, uses a circular 2π ramp phase mask, but it does not provide any depletion intensity towards the axial dimension. The latter, referred to as z-STED, uses a central circular area with a π-phase retardation, focusing its depletion on the axial direction. The combination of both masks has been developed, albeit incoherently, for an improved 3D STED imaging. The authors were able to tune the power distribution by use of a half-wave plate and a polarizing beam splitter (Harke et al., 2008). Both phase masks are shown in Figure 13.

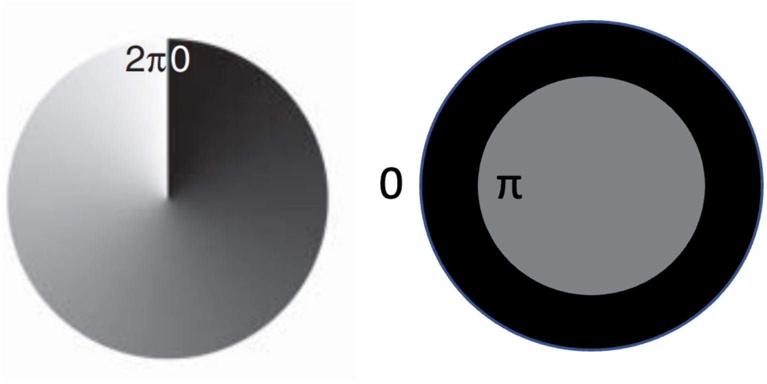

Figure 13: Profiles of depletion laser forming phase masks, 2D-STED featuring a circular 2π ramp phase mask (left) and z-STED featuring a central circular area with a π-phase retardation (right). Source: Adapted from (Gould et al., 2017)

1.6.2. Coherent-Hybrid STED

Coherent-Hybrid STED (CH-STED) is an alternative to improve the axial resolution in STED imaging through a variation of the common phase masks that shapes the depletion beam. This adjustment is expected to produce a long, narrow dip towards the Z dimension, while maintaining the depletion on the lateral dimensions. As previously mentioned, there have been two phase masks traditionally used to generate the depletion shape in the focal area: 2D-STED and z-STED. The proposed variation by the authors that produces the adjustment to the form of the depletion beam in the STED microscope is made possible through the coherent combination of the 2D-STED mask as an outer ring and a rescaled z-STED mask, producing a bi-vortex, as shown in Figure 14. The depletion areas in the 2D-STED mask, shown below on the left, are slightly dilated due to the overall rescaling to a radius below the unit circle value. The outer ring of the bi-vortex is of the same handedness as the inner vortex but out of phase. The radius at which the inner vortex changes phase with regards to the outer vortex is called rho (ρ) (Pereira et al., 2018).

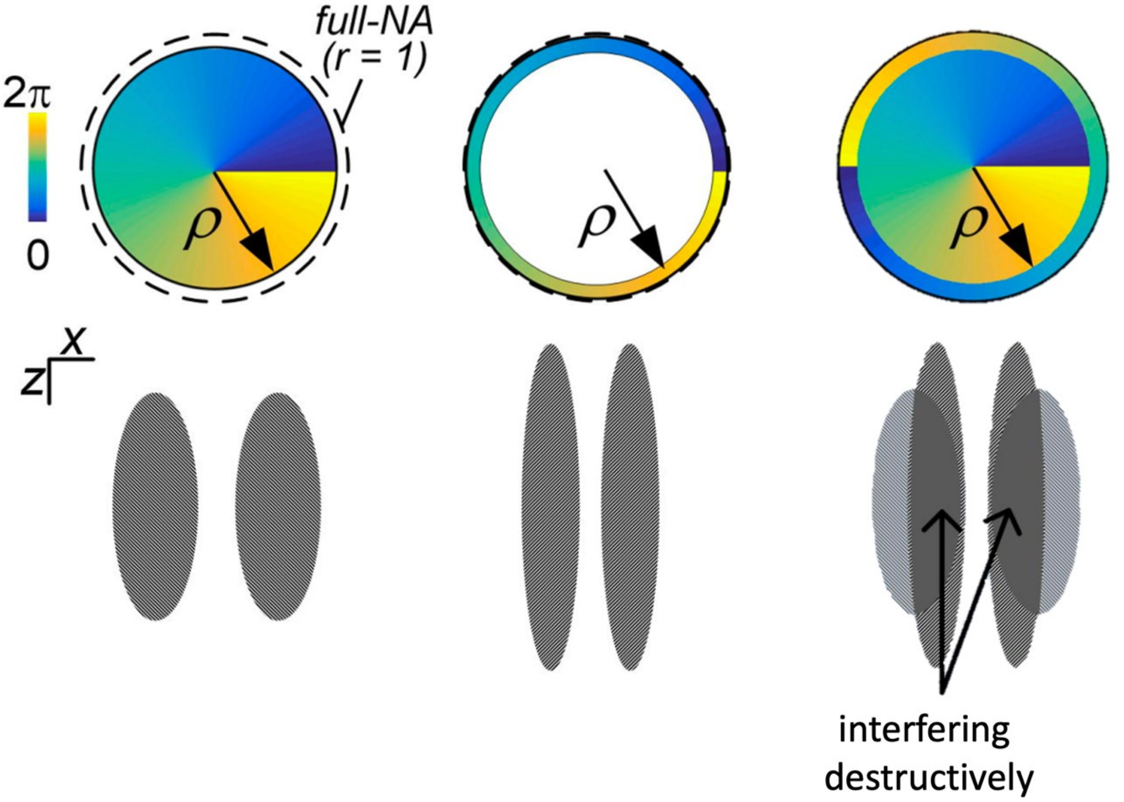

Figure 14: Top: The combination of the rescaled z-STED phase mask (left) with a 2D-STED mask outer ring (middle) resulting in the Bi-vortex phase mask representation (right). The dotted outer line in the left mask represents the unit circle, corresponding to a full numerical aperture vortex with a radius of 1. ρ corresponds to the rescaled z-STED mask radius. Bottom: Depletion areas created by each phase mask shown above. The rescaling of the z-STED mask slightly dilates its depletion areas. Their coherent combination provides a thinner central zero intensity area. Source: (Pereira et al., 2018)

As Sheppard and Hegedus state, a thin ring aperture is known to produce an extended constricted spot (Sheppard and Hegedus, 1988). Wang et al., describe an enhanced resolution in the lateral dimensions from applying an annular vortex in the depletion beam (Wang et al., 2017). The long, narrow dip, expected from the thin vortex implementation in the depletion beam is depicted in Figure 15. The volume of the dip is dependent on the inner radius ρ in the bi-vortex mask; a value that is modified through a graphical user interface (GUI) developed by the creators of the technique.

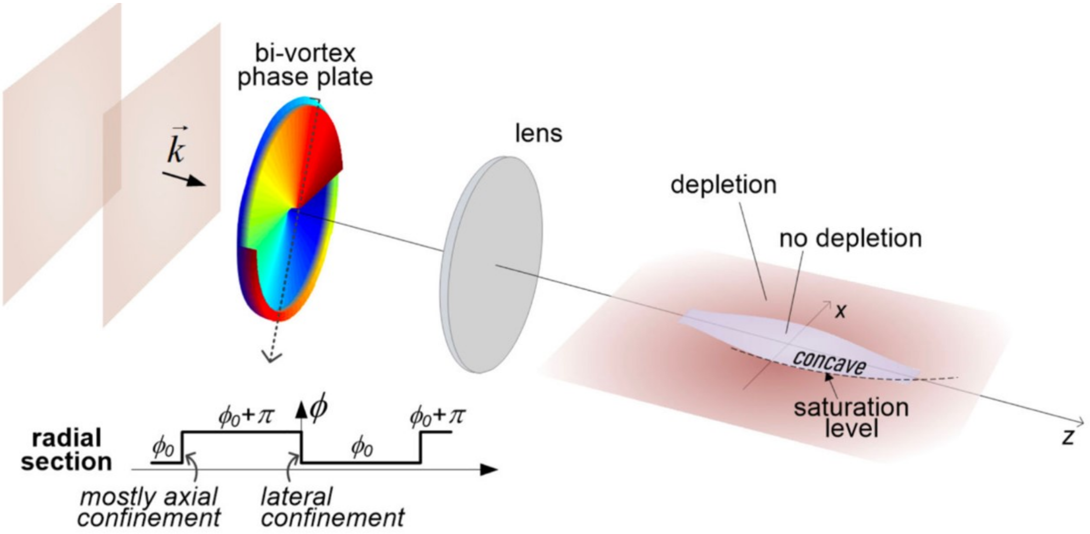

Figure 15: Simplified STED setup using the bi-vortex phase mask. The long, narrow dip is shown as a dotted line, towards the Z axis on the right side. A radial section is illustrated Source: (Pereira et al., 2019)

Pereira et al., claim the bi-vortex PSF is able to deplete the ghost spots from undepleted excitation lobes which are present during z-STED, and produce the expected dip which is non-existent during 2D-STED. Furthermore, the coherence of the bi-vortex aids in ensuring a depleted area of interest, as z-STED suffers from the possibility to fill the central zero-intensity area. The overall effect is understood as the suppression of out-of-focus fluorescence signal which improves imaging of complex samples. Moreover, the intensity of the depletion energy is redistributed along the Z axis, as the depletion lobes become elongated, allowing for higher intensities without the immediate consequence of photobleaching. Imaging of interphase cell and mitotic spindle samples was performed by the authors using a constant-power mode, and as an example, details such as signal from microtubules and fibers were only visible while employing CH-STED (Pereira et al., 2019).

2. MATERIALS AND METHODS

2.1. Software requirements

The CH-STED phase mask was developed through a Python script. To establish the connection between the microscope controlling software Imspector (16.3.16118-w2224, Abberior GmbH, Germany) and the CH-STED Python scripts, the Anaconda distribution software and the Specpy library were installed in the STED microscope workstation. The Anaconda distribution allows for the package management of Python in the workstation. The Specpy library is an in-house library developed by the microscope system developing company, Abberior, and requires the Numpy and Scipy libraries in the compatible Python release. The specifications were as follows: Anaconda 3 2021.11, Python language release 3.10.9, Numpy version 1.24.1, Scipy version 1.10.0 and Specpy version 1.2.3.

2.2. Test samples

2.2.1. Gold beads

The evaluation of the CH-STED masks was done using three samples. A testing sample consisting of gold nanoparticles (AuNPs) was developed (80nm, 1:500 in Mowiol, BBI Solutions, United Kingdom), although an Abberior-made sample (150nm, 1:5 in DPX, Abberior, Germany) was ultimately used. Even though the latter sample does not provide a defined lower resolution in the depletion beam profile due to the size of the beads, the former had issues concerning the background intensity and bead quantity in the specific dilution. The initial testing sample procedure consisted of a dilution of 1µl gold NPs into 500 µl 80% EtOH, from which 5µl were deposited on a glass slide and after evaporation, followed by 5µl of Mowiol (Kuraray, Germany) onto the gold NPs before positioning the coverslip. The gold beads were used for alignment purposes.

2.2.2. Crimson beads

A second sample was obtained from Abberior, comprising of crimson beads dyed with Alexa 647 (40nm, 1:5000 in Mowiol, Abberior, Germany). These beads were used for determining the depletion effect of the CH-STED phase mask at different rho values, focused mainly on the effective background depletion.

2.2.3. Mouse Embryonic Fibroblasts cells

A third sample was obtained from John Eriksson Lab, consisting of Mouse Embryonic Fibroblasts (MEF) cells, with vimentin phosphorylation site mutants stained with Abberior STAR 635. The structures of the cells were used to evaluate the effect of the CH-STED mask with regards to optical sectioning.

2.3. Microscopic imaging setup

All imaging was performed using a 2C Abberior STED microscope (Abberior, Germany) with an UPLSAPO oil immersion objective lens (N.A. 1.4, 100x, Olympus) in an Olympus IX83 microscope (Olympus, Japan). The optical path of the STED microscope is shown in **Figure 16**.

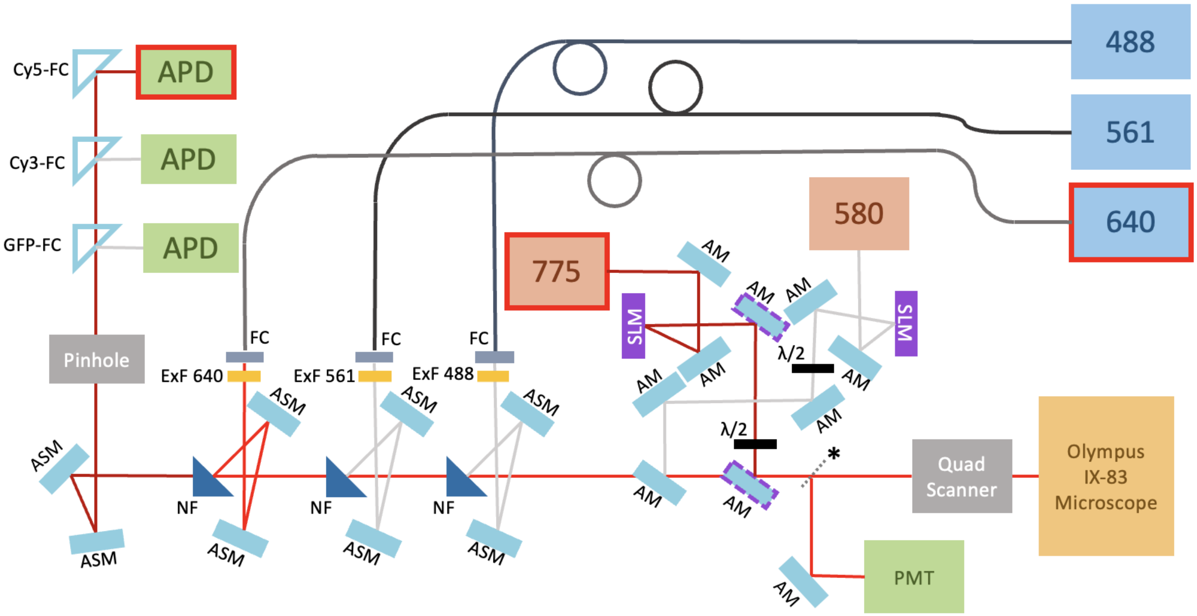

Figure 16: Optical path of STED microscope. Three excitation lasers, 488nm, 561nm and 640nm, and two depletion lasers, 580nm and 775nm, are available for imaging. Each depletion laser has a corresponding Spatial Light Modulator (SLM) for their phase modulation. The black components are λ/2 waveplates, for polarization altering purposes. A pinhole is located before the detection. Avalanche photodiodes (APD), on the top left, are the fluorescent detectors, with their corresponding filter cubes. A Photomultiplier Tube (PMT), on the lower right, is used for beam alignment purposes. (*) The pellicle is a movable component activated to alter the optical path when the PMT is chosen as detector. The scanning process is performed by the Quad Scanner, before connecting the optical path to the main body of an Olympus IX-83 microscope. AM stands for adjustable mirrors, and ASM for adjustable silver mirror. NF stands for notch filters, reflecting only certain wavelengths, and FC stands for fiber coupling. The purple highlight in two AM in the depletion beam modulation were adjusted by beam walking.

The gold nanoparticles sample was imaged using the reflection mode of the microscope, with the photomultiplier tube as the detector. To avoid under-sampling, the pixel size was 30nm in X and Z. The nanoparticles, or beads, behave as small mirrors, thus, they were used to reflect the excitation and depletion beams for proper alignment. A single gold bead was imaged in XZ plane with no depletion mask to align the depletion beam with respect to the Z axis. This vertical alignment was performed by fine-tuning the adjustable mirrors with purple highlight in Figure 16 located in the depletion beam path after its corresponding SLM (Hamamatsu, Japan) and before the beam would enter the Olympus microscope. This procedure is also known as beam-walking.

Agha and Minkin, (2007) explain the process of beam walking in a simple optical setup involving a laser source, two adjustable mirrors in X and Y and two irises as pinholes opened enough to allow the laser to pass through them. The setup is shown in Figure 17. Mirror 1 is called the position mirror as its adjustment mainly affects the positioning of the laser beam at the first pinhole, and mirror 2 is the angle mirror, since it mainly affects the angle of the laser beam as it reaches the first pinhole. In practice however, the effect of the adjustment of mirror 1 is observed in pinhole 1, and the adjustment of mirror 2 in pinhole 2. The iterative adjustments on each mirror aim to ensure the centering of the laser beam with regards to the pinholes.

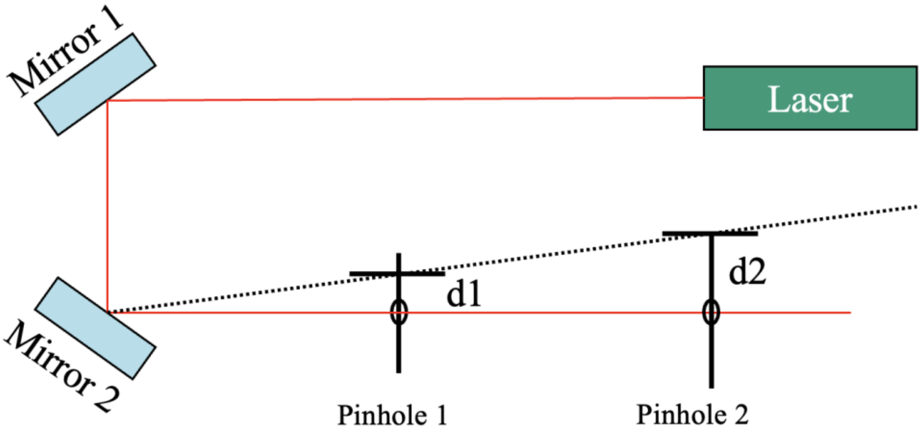

Figure 17: Optical setup for beam walking procedure. d1 and d2 are the distances at which the laser beam is misaligned from the pinholes. Source: Adapted from (Agha and Minkin, 2007)

In the STED microscope, the process for beam walking would initially require the phase mask of the depletion beam to be shut off to evaluate the tilt in Z. Then, for instance, a slight tuning of mirror 1 in the X axis could be performed with a return in mirror 2 in the same axis, followed by a verification of the adjustment effect on the tilt. Additional repetitions of this procedure could be required.

Afterwards, the 2D-STED phase mask was used to align the 640nm laser in the XY and XZ planes. The Imspector software contains different tool windows which enable control of specific components of the microscope. These windows are called Live Dialogs. The 775nm depletion beam was adjusted with the corresponding Live Dialog where the offset and gratings values of the phase mask are regulated to align the excitation and depletion beams.

Further, the CH-STED GUI python code was run using the Anaconda 2022.10 Powershell Prompt. The GUI consists of 5 features to produce the depletion mask, yet all values except one were left unchanged from default, following the authors comments. The modified feature, called rho, dictates the radius where the inner vortex of the mask changes sign; the authors note a value of 1.0 is effectively equivalent to using the 2D phase mask. The expected shape of the depletion beam using the CH-STED mask is shown in Figure 18.

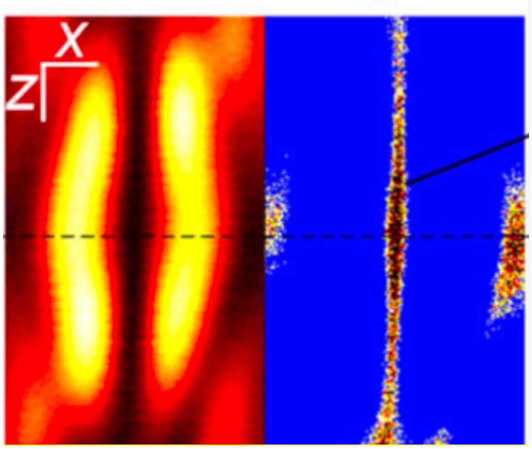

Figure 18: (left) Expected shape of depletion beam in the XZ plane using the CH-STED mask; (right) Expected depletion effect from the mask onto the fluorescent sample. Source: (Pereira et al., 2019)

In addition to the depletion beam adjustments using the Live Dialog, other parameters were modified to follow the CH-STED specifications according to the authors. The pinhole, component which is used to filter emission light from out of the focus plane in the sample, was set at 0.88 Airy Units to obtain better optical sectioning. Moreover, the Avalanche photodiode detectors from the microscope structure were set with a timed gating starting at 1.40ns until 8ns, enabling the detection to be performed at a delay ensuring the depletion of the surrounding fluorophores has occurred.

2.3.1. Python script calibration

The Python script developed by the authors featured a value name “Unit Circle”, shown in Figure 19, which corresponds to the number of pixels in the SLM. This value should be tested and calibrated for every STED microscope setup in which the CH-STED phase mask is used, as it is also dependent on the diameter of the depletion beam and the back aperture of the objective from the system. The initial testing of the CH-STED phase mask did not produce the phase modulation expected from the original work; thus, the unit circle value was modified. The default value was 108 pixels, and it was intentionally lowered to observe the effect of the phase mask. At a range of 60-70 pixels, the phase mask was producing a similar response to the expected, thus 65 pixels was chosen as a starting point for further calibration.

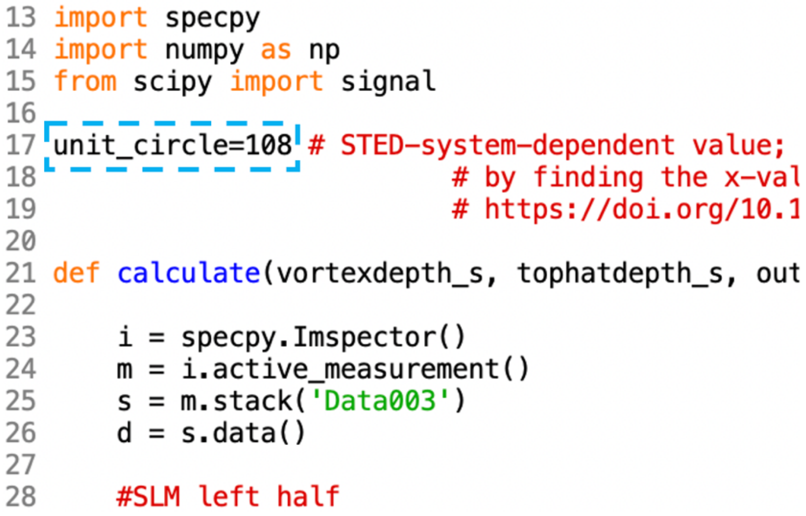

```
import specpy
import numpy as np
from scipy import signal

unit_circle=108 # STED-system-dependent value;
                         # by finding the x-val
                         # https://doi.org/10.1

def calculate(vortexdepth_s, tophatdepth_s, out

    i = specpy.Imspector()
    m = i.active_measurement()
    s = m.stack('Data003')
    d = s.data()

    #SLM left half
```

Figure 19: Excerpt from Python script from which the "Unit Circle" calibration is established. The comment on the right reads as follows: “STED-system-dependent value; must do some calibration, such as finding the x-value of the discontinuity in Fig2c inset in paper https://doi.org/10.1364/OE.27.008092”. Source: (Pereira et al., 2019)

After proper alignment with the excitation beam using the gold beads sample, the depletion beam was imaged at a range of rho values, from 0.80 to 1.10 with a step of 0.02 on multiple gold beads. The focal plane of the depletion beam was established by averaging the size of the excitation beam and translating the plane to the corresponding depletion beam images. The profile drawn on the focal plane was plotted using the open-source image processing software ImageJ/Fiji, to display the intensities of the pixels versus the distance in nm along the plane. **Figure 20** depicts the analysis of the profile with 2D-STED and CH-STED of one gold bead.

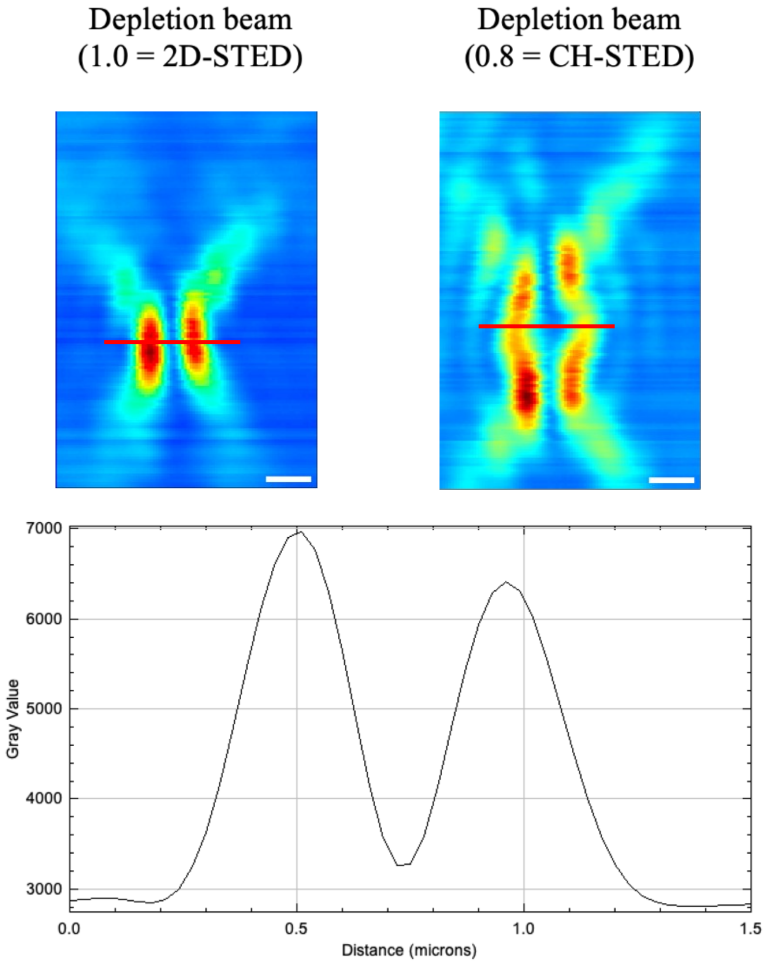

Figure 20: (above) XZ depictions of the depletion beam with rho values at 1.0 and 0.8, demonstrating 2D-STED and CH-STED respectively, with profiles drawn at their focal plane. (below) Graphical representation of profile of the focal plane distribution of the depletion beam with 2D-STED using Fiji/ImageJ. Scale bar: 0.5μm

Each plot was then fitted to a parabolic approximation, focusing on the midpoint between the depletion beam lobes, for determining the coefficients through an R language script, where f(x) corresponded to the intensity values and the x to the distance values. **Figure 21** illustrates the process through the R script to determine the midpoint of the focal plane profile of the depletion beam with 2D-STED, and the fitting of the second-degree polynomial.

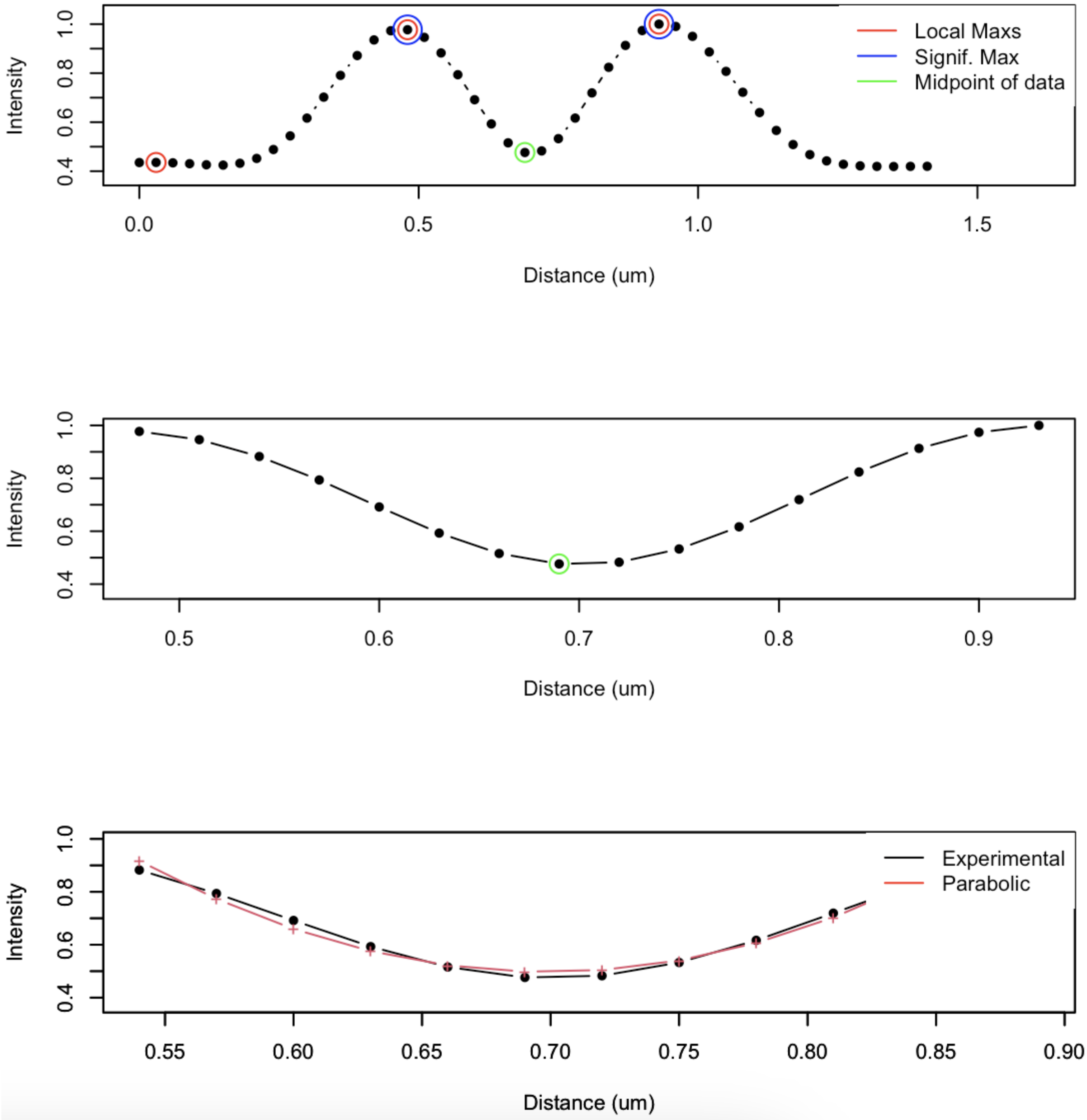

Figure 21: Graphical representation of the fitting of the second-degree polynomial using a script in R. (above) Plotting of the focal plane profile of the depletion beam, and designation of the local maximas of the lobes in red/blue, and midpoint in green. (middle) Sectioning of the graph, focusing in the range between the maximas of the profile. (below) Parabolic fitting to the sectioned range of the graph. The coefficients of the polynomial were saved for further analysis.

Subsequently, the coefficients of the second-degree variable of each fit were graphed, resulting in a curve, shown in **Figure 22**. The inflexion point, the value at which the growth of the curve became stable, was multiplied to the original unit circle value where the resultant should be used as the pixel size.

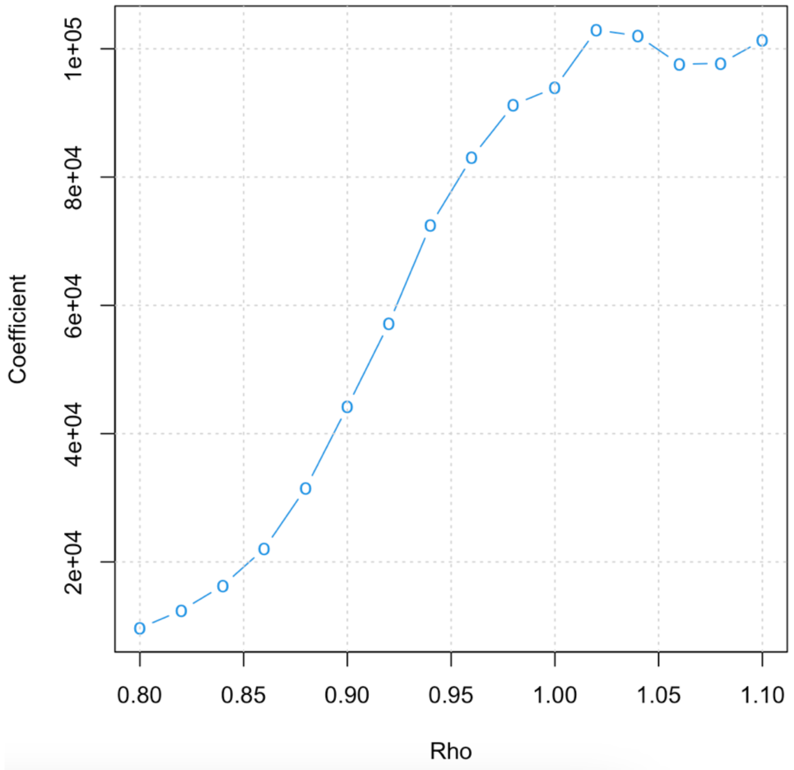

Figure 22: Graph of the coefficients of the second-degree variable. The inflexion point of the growth (point at which the growth becomes stable) is to be determined and multiplied to the Unit Circle value in the mask generating Python script. The result of the multiplication is the calibrated Unit Circle value.

The previously described analysis was performed on multiple gold beads. A single bead was chosen to depict the shown figures. The inflexion point in the analysis of this specific bead was determined between 1.00 and 1.05, therefore, the original estimation was quite accurate.

2.4. Sample Imaging

The crimson bead sample, consisting of dispersed fluorescent nanospheroids, was imaged using the 640nm excitation laser, the Cy5 filter set, and the Avalanche Photo Diode (APD) detector in the 650nm-720nm range. The MEF cells sample was imaged using the same excitation light, filter, and detector configuration. The depletion beam utilized was the 775nm, with its corresponding SLM for phase modulation.

Two groups of several crimson beads, at different rho values from 0.8 to 1.0, were imaged in the XZ plane, to evaluate the resultant depletion effect after proper gold bead alignment and unit circle calibration. The pixel size was 20nm in X and Z. Next, single slices and a stack of the MEF cell samples were imaged at the same range of rho values, from 0.8 to 1.0. The pixel size in the single slices was 20nm in X and Y. The pixel size in the image stack was 20nm for X and Y and 150nm in Z. In all imaging experiments, the Line Step acquisition mode was chosen with 1 and 3 line step accumulations for Confocal and STED respectively. Image analysis was performed using the open-source image processing software ImageJ/Fiji.

2.5. Image Analysis

Several crimson beads were selected and compared throughout the changes in rho (at 0.8, 0.84, 0.9-0.92 and 1.0) by determining the lateral resolution through measuring the Full Width at Half Maximum (FWHM) of their respective PSFs at the focal plane and at a Rayleigh distance (260nm). The FWHM measurement requires the plot of the focal plane profile of the bead, at which a Gaussian function is fit, and the width of the fit at half the maximum corresponds to the resolution of the bead. Profiles of the single slices and of the MEF cell sample were drawn and plotted to observe the respective photocount with the depletion beam phase mask at 0.8 (CH-STED) and 1.0 (2D-STED). The maximum intensity power for the depletion beam available was 1.1W, and the crimson beads and MEF cell sample were imaged at intensities of 10% and at a range of 14-16%, respectively. However, the percentages are in a non-linear variation. Furthermore, the intensity of the depletion beam was measured at the laser head, where 10% corresponded to 106mW, 14% to 150mW and 16% to 170mW.

3. RESULTS

3.1. Crimson bead imaging with evaluation of PSF

The CH-STED phase mask with a rho value of 1.0 effectively produces the same depletion result as in 2D-STED. The crimson bead sample was imaged at different rho values modulating the respective phase mask to analyze the effect of the depletion beam comparing 2D-STED to CH-STED, shown in Figure 23.

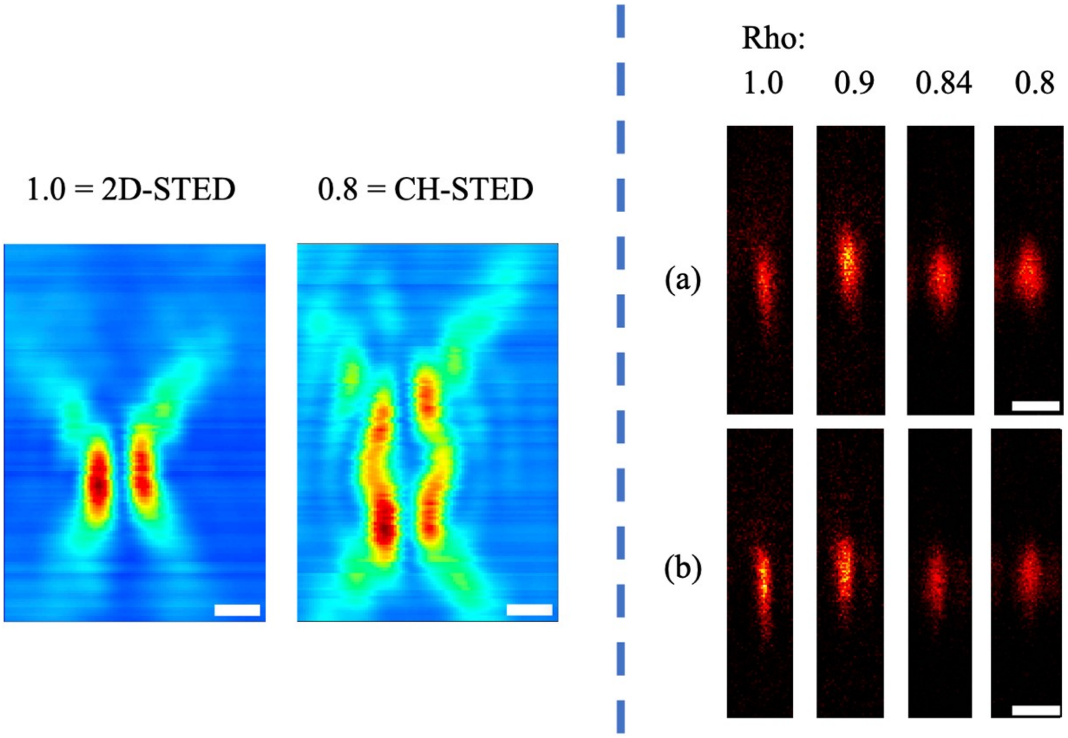

Figure 23: (left) Gold bead imaging showing 2D-STED and CH-STED depletion beams. (right) Two crimson beads imaged at XZ plane, at different rho values. Scale bar: 0.5µm

There is compression in the axial dimension of the crimson beads as the rho value approaches 0.8. This reflects the desired dip in CH-STED, expected from the original publication, leading to a suppression of out-of-focus signal not feasible in 2D-STED.

Figure 24 displays the PSF analysis through FWHM of a crimson bead using 2D-STED (at 1.0) and CH-STED (at 0.84) at the XY plane to illustrate the decline in lateral resolution when using the latter phase mask.

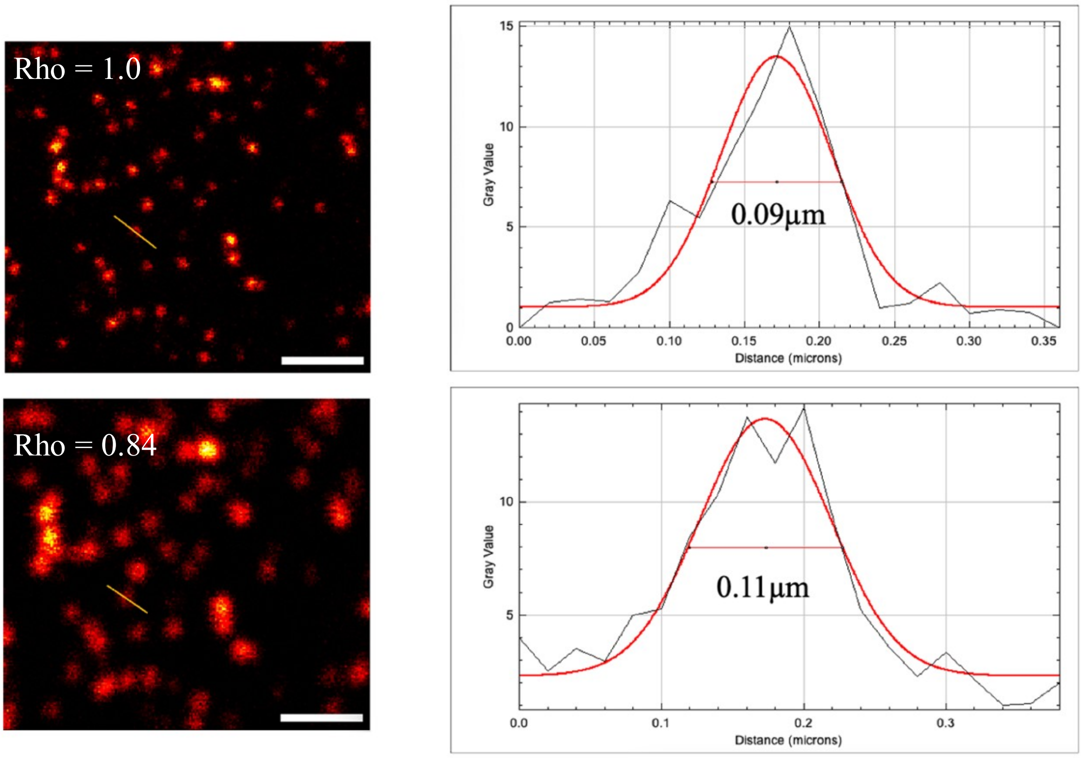

Figure 24: PSF analysis of a midplane of a crimson bead using 2D-STED (at 1.0) and CH-STED (at 0.84). The profile drawn at the focal plane and the subsequent graph were done using ImageJ/Fiji. Scale bar: 1µm

Figure 25 further illustrates this decline through the trends of lateral resolution in one crimson bead at different depletion laser power intensities over four different rho values. The FWHM measurement was performed at the same midplane in all combinations.

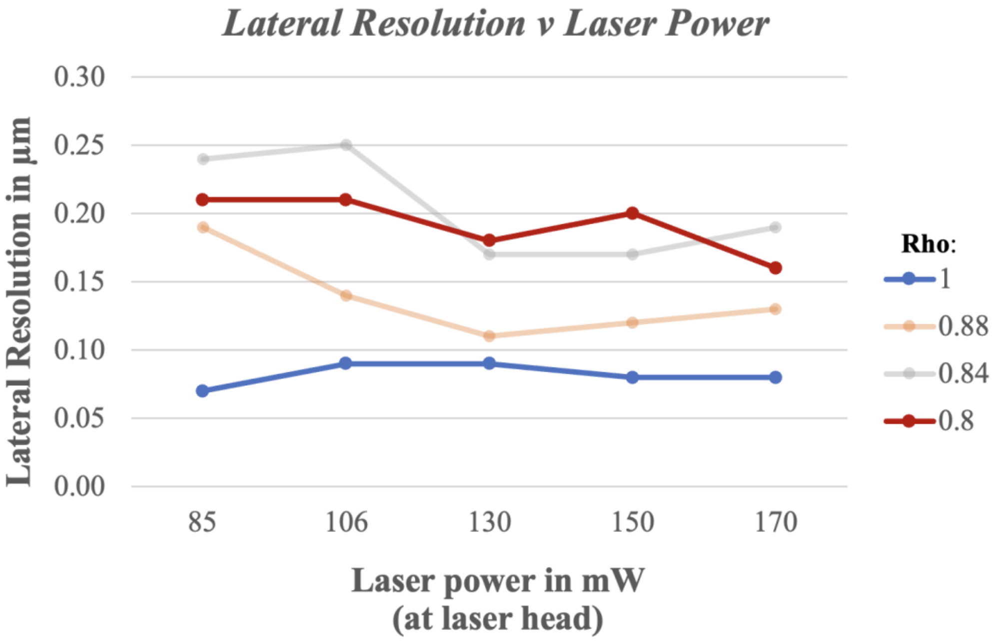

Figure 25: Trends of the lateral resolution of a crimson bead at increasing depletion laser intensities with corresponding depletion masks at different Rho values. The laser power

intensity was measured at the laser head. The FWHM measurement was performed at the same midplane on all bead combinations using ImageJ/Fiji.

The PSFs of 5 sets of multiple crimson beads were measured at the focal plane and the Rayleigh length of the laser beam (0.26µm from focal plane), through the FWHM procedure at different rho values to determine the background suppression effect of the mask. The Rayleigh length is a distance at which the excitation laser beam doubles its area of focus. Figure 26 shows the trends of such measurements.

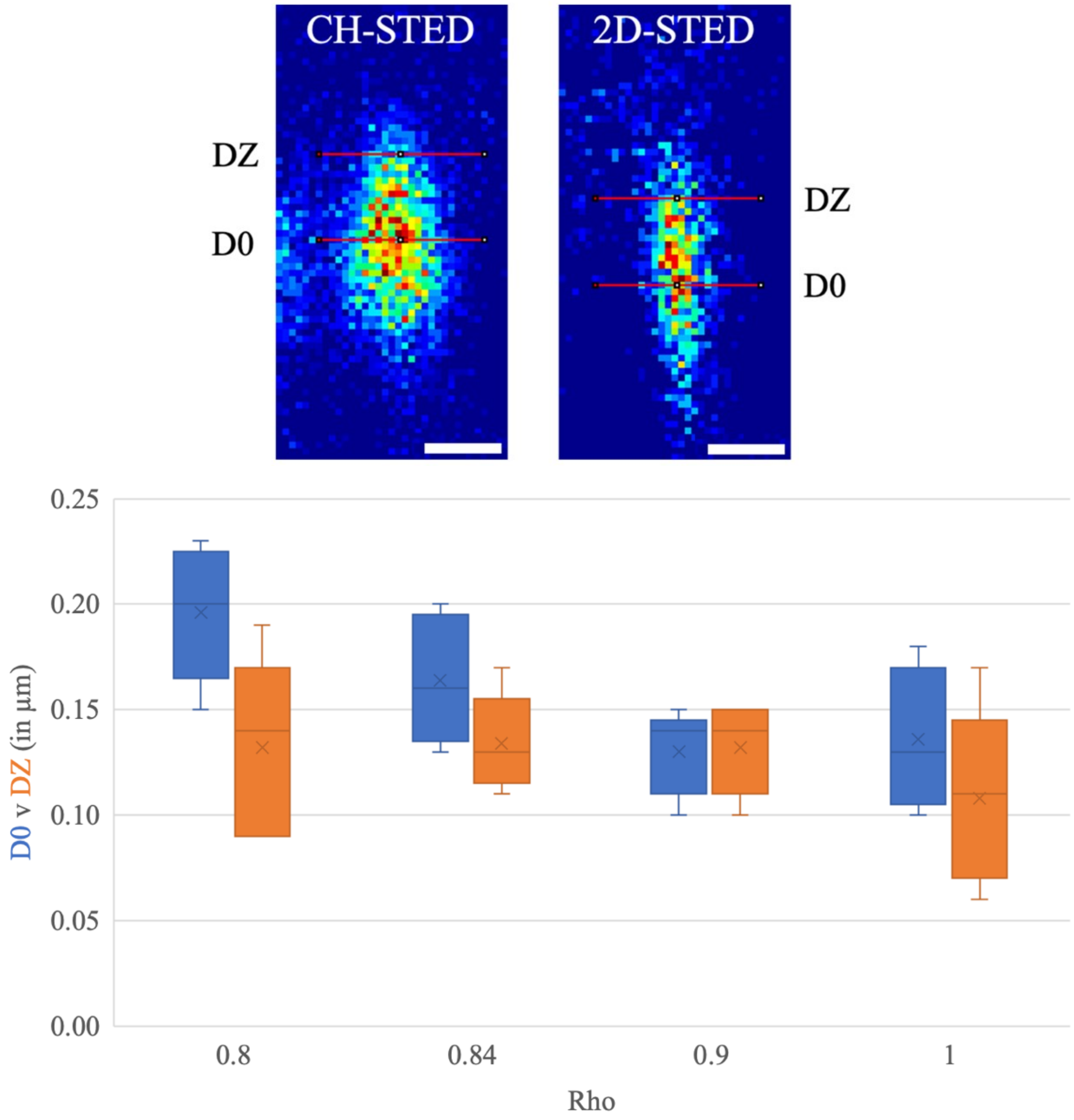

Figure 26: (above) Crimson beads with CH-STED and 2D-STED illustrating the focal plane (D0) and Rayleigh length (DZ) for PSF measurement using ImageJ/Fiji. (below) Graphical representation of the width of the beads at focal plane and Rayleigh length to determine background suppression effect. Scale bar: 0.3µm

The trend of the measurements at D0 (focal plane) show an increase in size as the rho value of the phase mask reaches 0.8 from 1.0. Meanwhile, the trend of the measurements at DZ (Rayleigh length) illustrate a constant lateral distance, from rho value of 1.0 towards 0.8. The widths of the beads in DZ for 0.8 and 1.0 showed wide variation unlike in rho values for 0.84 and 0.9.

3.2. Comparison of Mouse Embryonic Fibroblasts cells

Orthogonal views of the image stack of a Mouse Embryonic Fibroblasts (MEF) cell with stained vimentin phosphorylation site mutants are shown in Figure 27. The XZ and YZ planes provide a side view of the sample to observe the depletion effect of the mask with regards to the thickness of the sample. There is a noticeable contraction in the axial plane of the filaments, labeled with a curly bracket in the XZ and YZ planes at the bottom and right sides of Figure 27, providing a significant improvement in optical sectioning in CH-STED, as was seen in the crimson bead sample analysis. A moderate loss in lateral resolution is noticeable in CH-STED compared to 2D-STED, however it was expected from the behavior of the depletion beam mask seen in Figure 23 and Figure 24. Additionally, the signal in the lateral views of CH-STED appears concentrated unlike the diffuse behavior along the Z axis within 2D-STED.

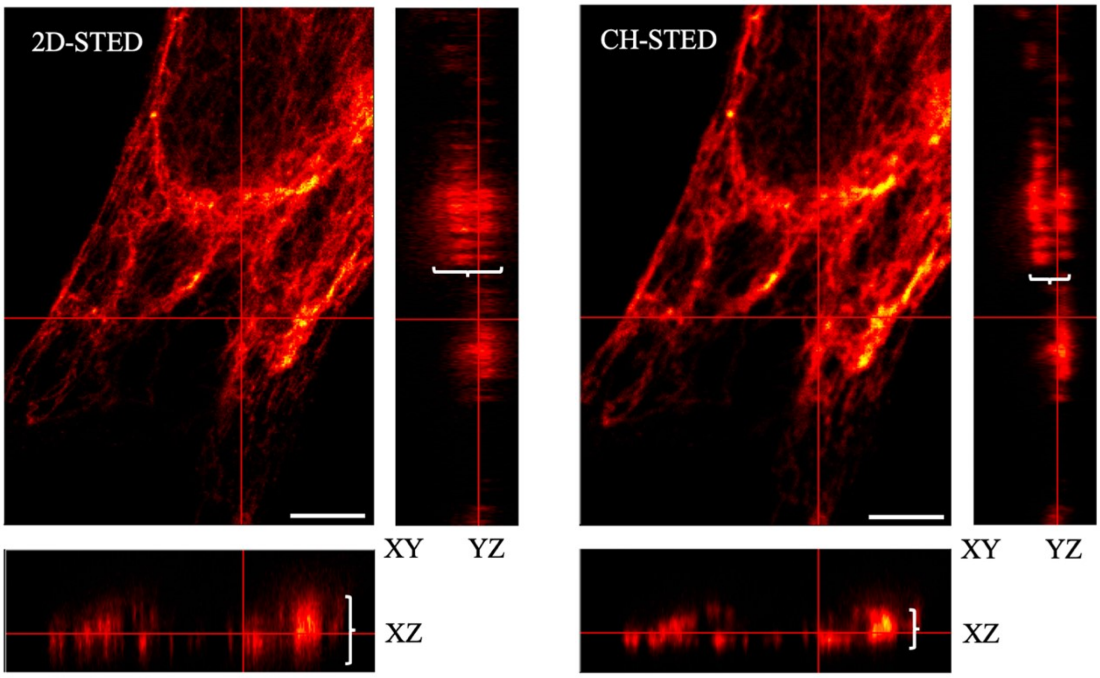

(Figure 27 continues in the next page)

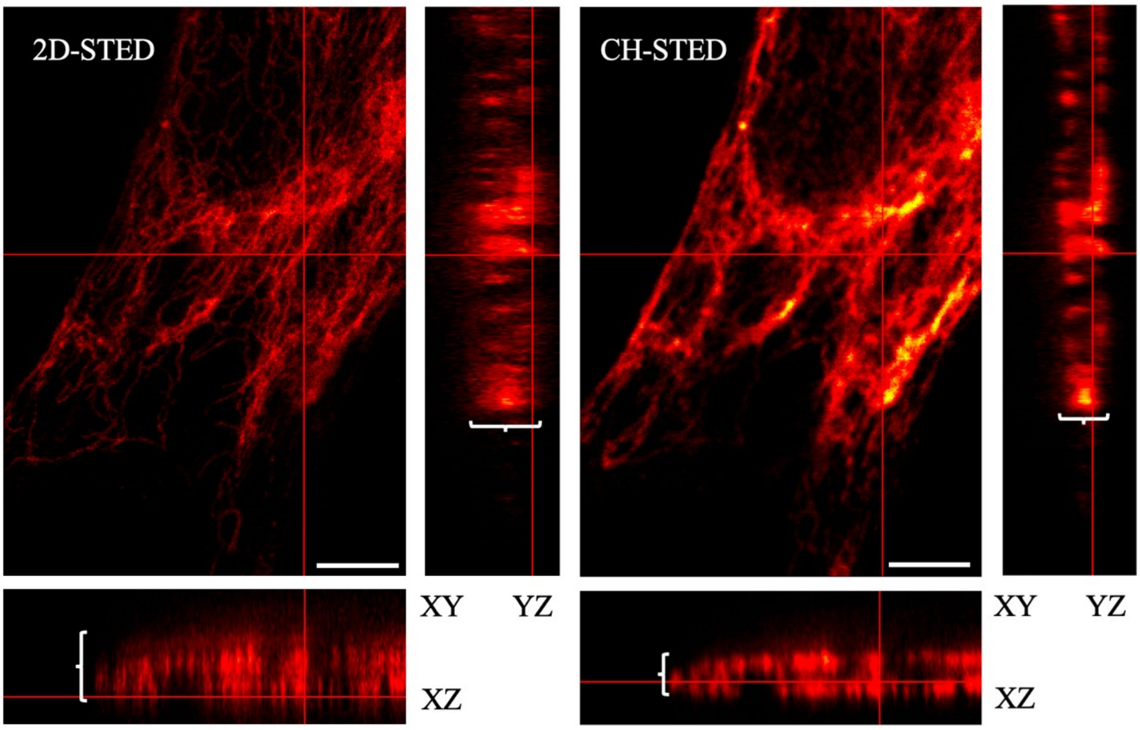

Figure 27: Orthogonal views of 2 image stacks of the MEF cell sample. XZ and YZ views are on the bottom and right side of each XY plane, respectively. Curly brackets in the XZ and YZ planes indicate the axial contraction of CH-STED compared to 2D-STED. Scale bar in XY plane: 3μm

A general comparison of a MEF cell, imaged with 2D-STED and CH-STED respectively, is shown in Figure 28. The excitation and depletion laser beams intensities and the detection gating were consistent for all imaging sessions. Certain filament details of the cell are removed in CH-STED, while the observable details possess apparent higher intensities than in 2D-STED.

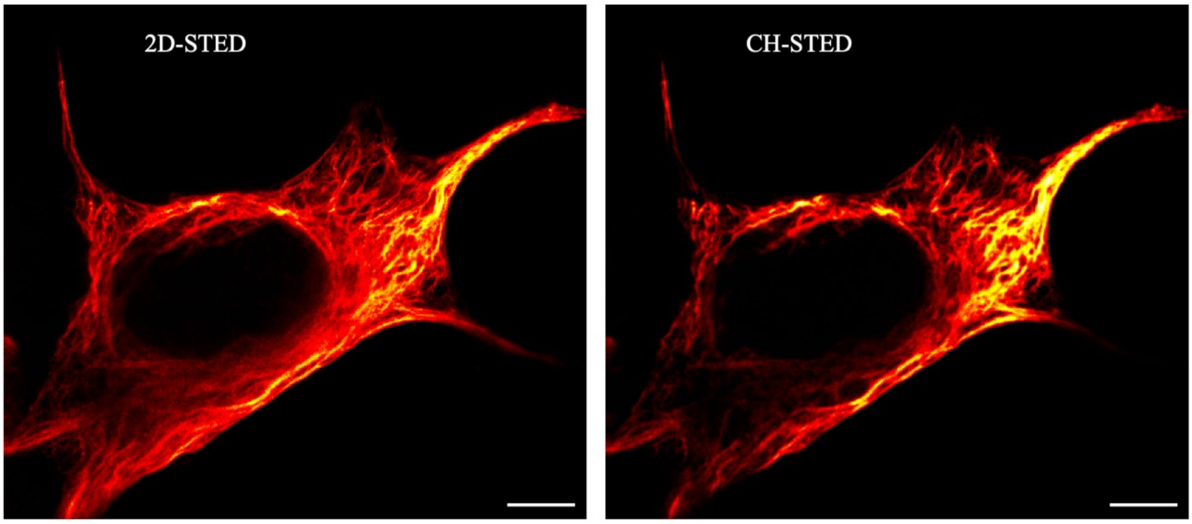

Figure 28: MEF cell sample comparison, between 2D-STED and CH-STED. Scale bar: 5μm

Several profiles from the single slice images of the MEF cell sample were plotted with 2D-STED and CH-STED, respectively. Once again, a loss in lateral resolution is evident. Figure 29 and Figure 30 show the location of the plot drawn in each sample and the resulting Distance v. Intensity graphical representation. The chosen structures display several filaments which provide a series of comparisons between signal and background. The resulting graph illustrates an increase in signal, and contrast with regards to the background fluorescence, from the CH-STED profile in both instances. However, the noise in the signal is maintained. The order in which the phase masks are imaged can influence the intensities of the acquired signal, due to photobleaching of the sample. Nevertheless, in the following examples, the order was alternated, and no significant difference or photobleaching effects were encountered.

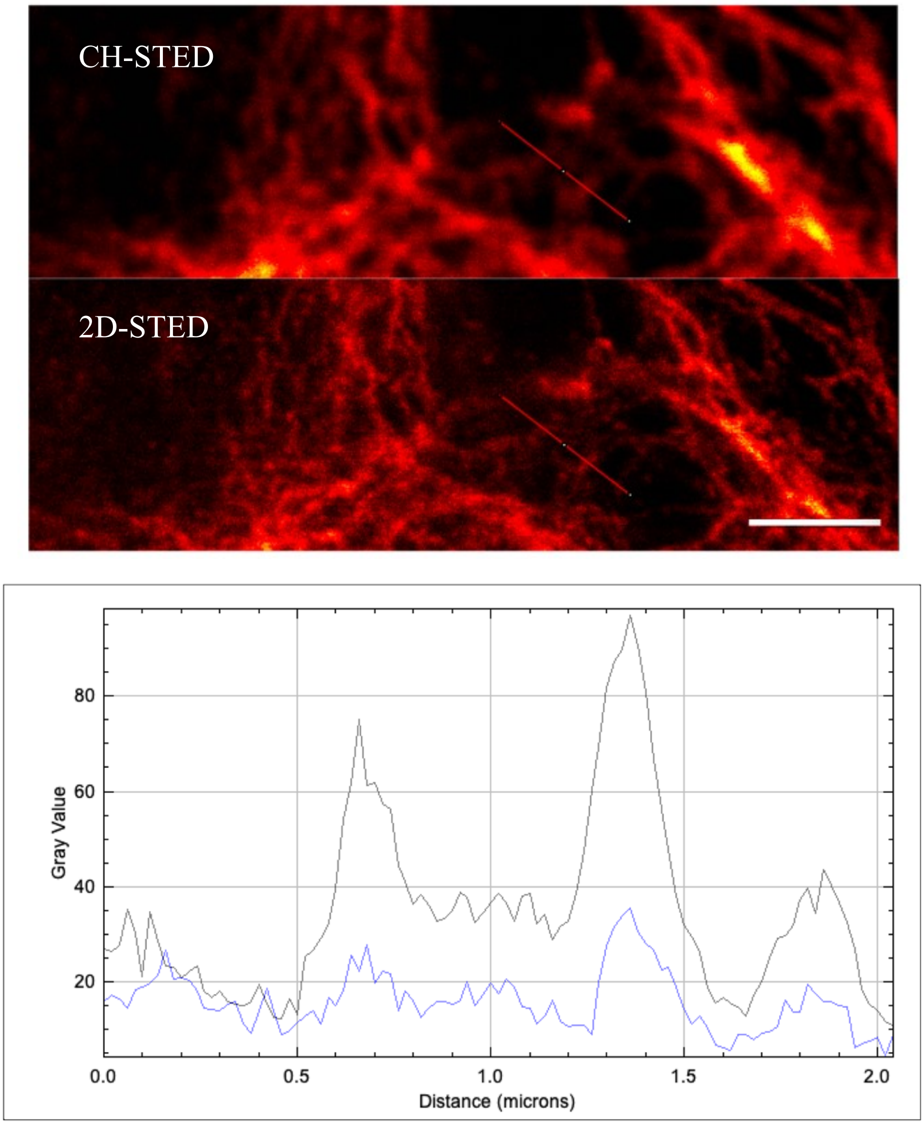

Figure 29: Profile plot from single slice image of MEF cell sample, with rho values at 0.8 (top half) and 1.0 (bottom half). In the graph, the blue line represents the profile drawn in 2D-STED,

and the black line represents the profile drawn in CH-STED. The excitation and depletion laser beams intensities and the detection gating were consistent for all imaging sessions. Intensity of depletion beam was set at 14%, corresponding to 150mW when measured at the laser head, to avoid notable photobleaching. Scale bar: 2µm

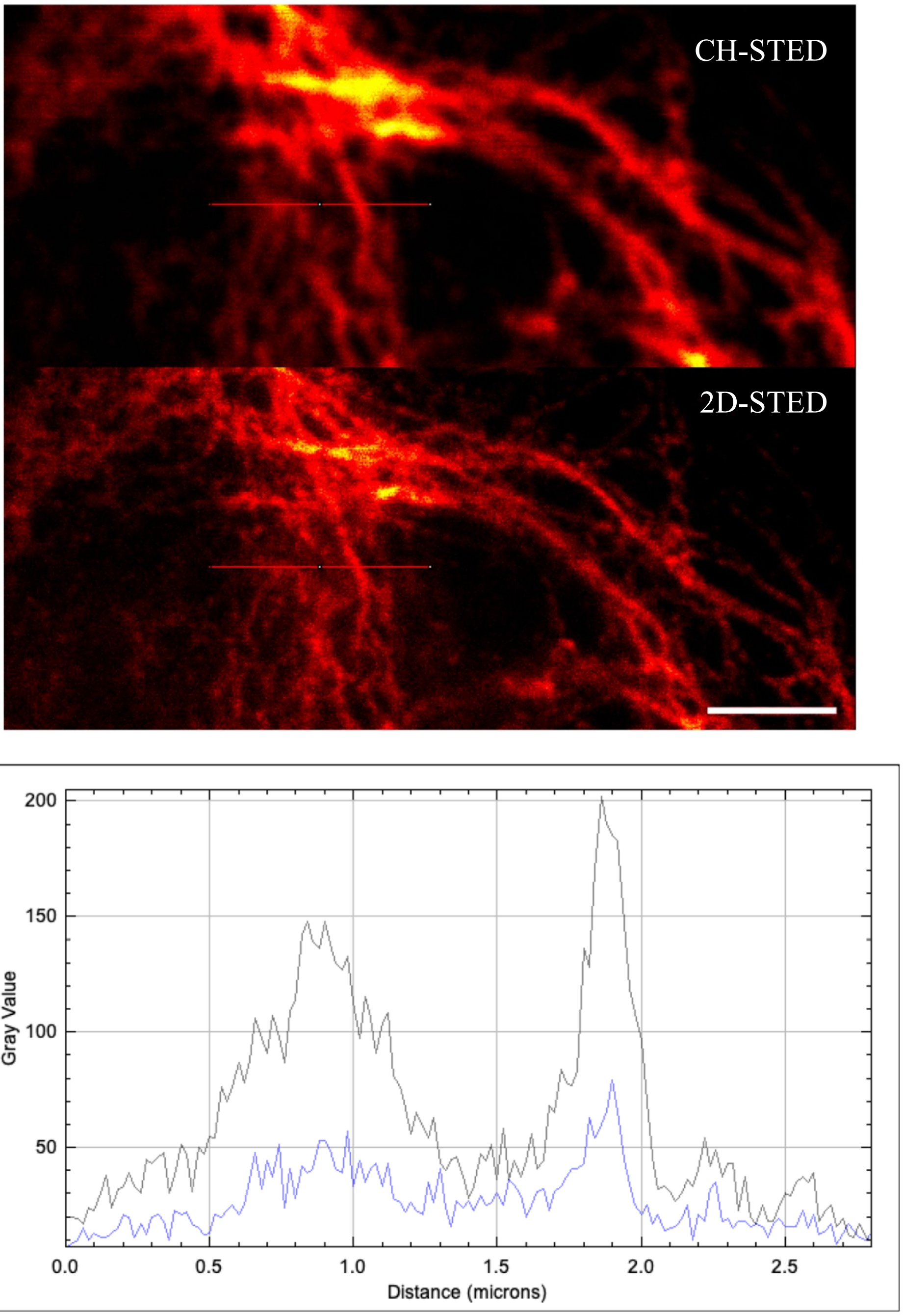

Figure 30: Profile plot from single slice image of MEF cell sample, with rho values at 0.8 (top half) and 1.0 (bottom half). In the graph, the blue line represents the profile drawn in 2D-STED, and the black line represents the profile drawn in CH-STED. The excitation and depletion laser beams intensities and the detection gating were consistent for all imaging sessions. Intensity of depletion beam was set at 14%, corresponding to 150mW when measured at the laser head, to avoid notable photobleaching. Scale bar: 2µm

Additional views of a different MEF cell are shown in Figure 31. The thickness of the cell can be observed as both images were taken at different planes. The bottom image represents the structures found in the middle region of the top image. Figure 32 shows the plot profile of a single slice image of the structures of the cell in the bottom half of Figure 31. Details from the outer region of the cell are filtered out from the CH-STED image as compared to 2D-STED. The difference in intensity values from both masks are also depicted, where the red line represents the profile drawn in CH-STED and the black line corresponds to the profile drawn in 2D-STED.

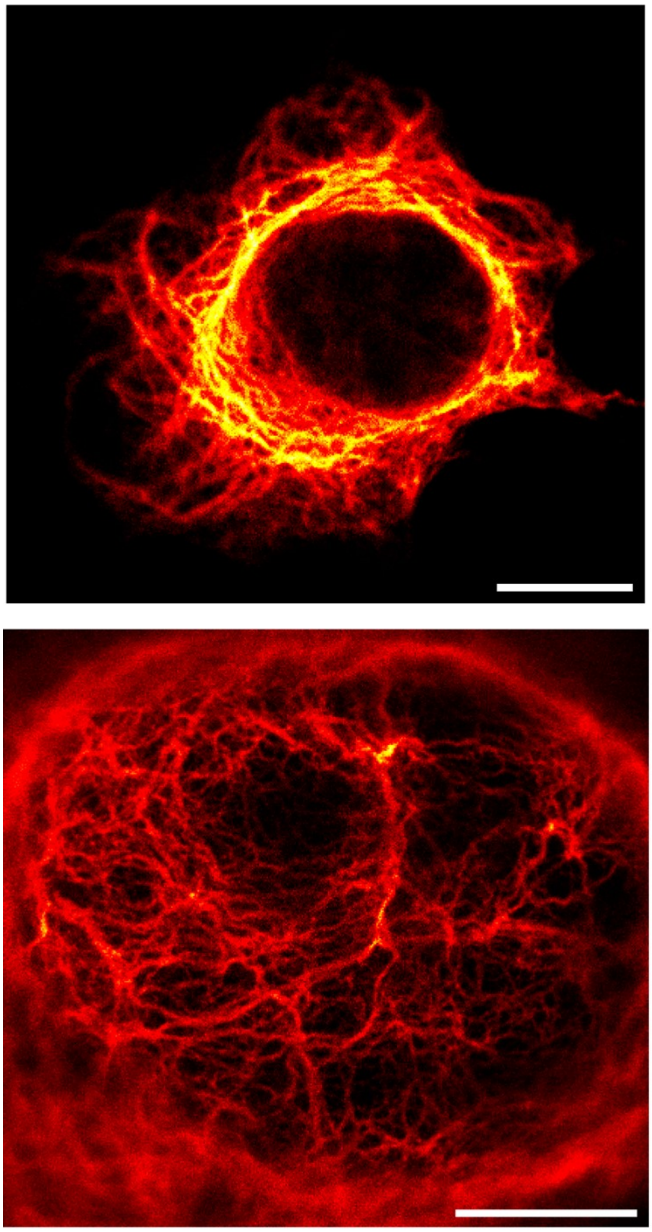

Figure 31: MEF cell sample comparison, between 2D-STED and CH-STED. Scale bars: (above) 10µm and (below) 5µm

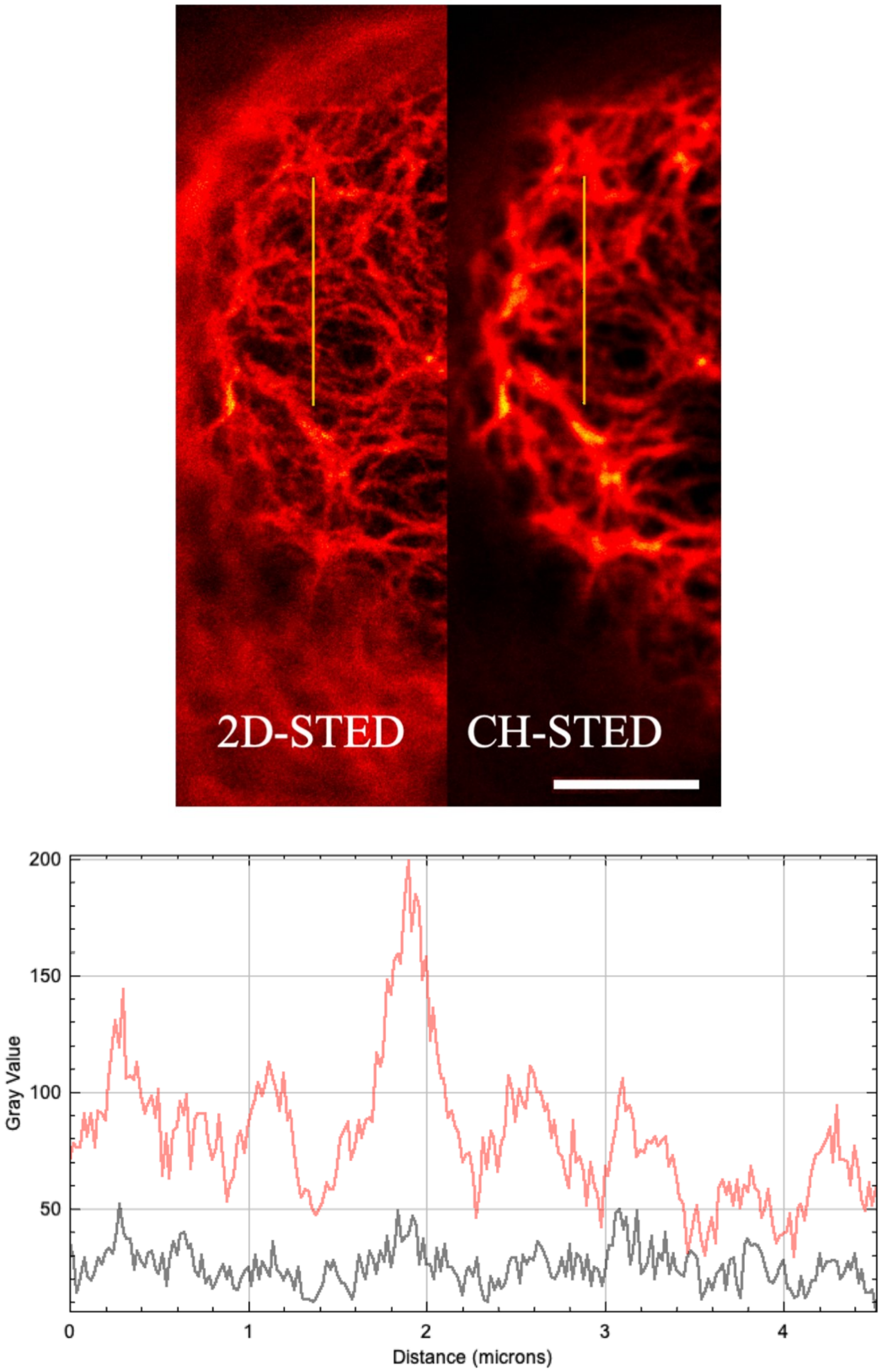

Figure 32: Profile plot from single slice image of MEF cell sample, with rho values at 1.0 (left) and 0.84 (right). In the graph, the red line represents the profile drawn in CH-STED, and the black line represents the profile drawn in 2D-STED. The excitation and depletion laser beam intensities as well as the detection gating were consistent for all imaging sessions. Intensity of the depletion beam was set at 16%, corresponding to 170mW when measured at the laser head, to avoid notable photobleaching. Scale bar: 3µm

In Figure 33, the Maximum Intensity projection of an image stack of the MEF cell sample is shown, along with a drawn profile to depict any intensity changes between 2D-STED and CH-STED. Similar to the previous profiles in the single slices of the MEF sample, the signal in CH-STED is apparently higher than in 2D-STED, however, the change in intensity is not as severe. The noise is still maintained in both images.

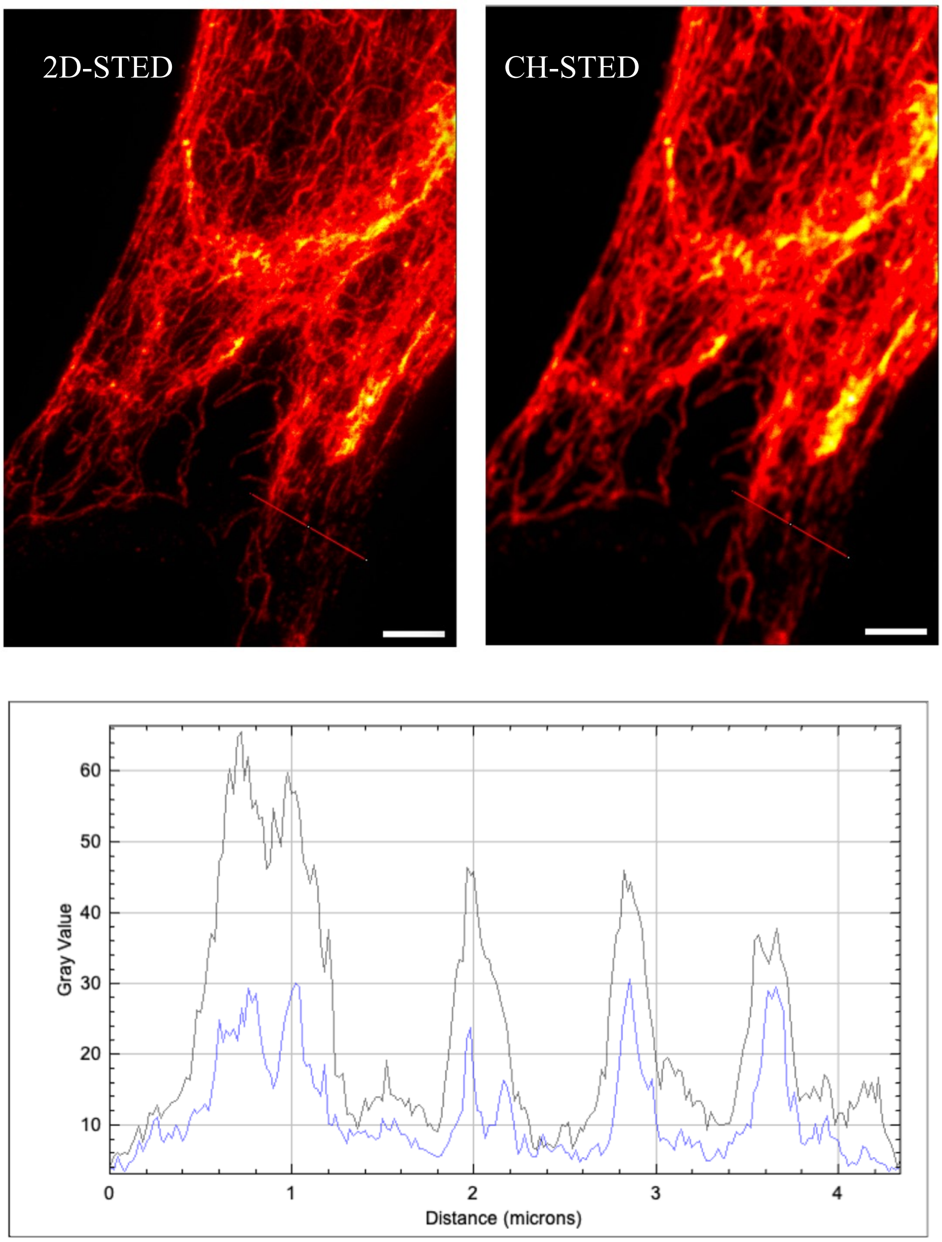

Figure 33: Profile plot from a Maximum Intensity Projection of an image stack of MEF cell sample, in 2D-STED (left) and CH-STED (right). In the graph, the blue line represents the profile drawn in 2D-STED, and the black line represents the profile drawn in CH-STED. The excitation and depletion laser beams intensities and the detection gating were consistent for all imaging sessions. Intensity of depletion beam was set at 14%, corresponding to 150mW when measured at the laser head, to avoid notable photobleaching. Scale bar: 4μm

4. DISCUSSION

Troubleshooting is required during the initial connection of the Python script and the STED microscope software. Changes in the updates of the utilized general Python libraries, in addition to the main functions of the connection library (Specpy) between the coding language and the imaging control software can result in errors, for which a general understanding of the code development and connectivity process is required. The calibration of the Unit Circle is essential to properly observe the effects of the CH-STED mask on the resulting image. A wider explanation of this process, for instance available at Pereira et al., (2019), could simplify the implementation of the phase mask to new users, without the need to consult with the original authors.

Regarding the individual crimson bead comparison at different rho values in the phase mask, there is a noticeable contraction in the axial dimension as the rho value decreases towards 0.8. However, a growth in size at the lateral dimension of the focal plane can also be perceived, due to the widening at the center of the depletion beam, which can be observed in the left portion of Figure 23, leading to a loss in lateral dimension which was expected according to Pereira et al., (2019), graphically depicted in Figure 24 in the XY plane.

The trends of Figure 25 illustrate the loss in lateral resolution in the crimson bead as the rho value decreases. However, a slight increase in resolution is apparent as the depletion laser power increases in each of the rho values lower than 1.0, which can be attributed to the additional depletion laser energy distributed along the lateral plane.

In the graphical representation of the lateral dimensions at the focal plane (D0) and Rayleigh length (DZ) in Figure 26, following the trend of D0 from right to left, the increase in size corresponds to the widening behavior of the depletion mask previously discussed. Meanwhile, the average of the width of the beads at DZ stays consistent from 1.0 to 0.8.

The side views from planes XZ and YZ of the MEF cell sample shown in Figure 27 properly illustrate the enhanced optical sectioning from the depletion effect of CH-STED, as the details of the cell appear constricted and focused. Nevertheless, the lateral dimension is once again at an expected loss, due the nature of the mask.

In Figure 28 and Figure 31, the MEF cell displays an apparent loss in signal in CH-STED compared to 2D-STED, however this behavior is not a loss but a filtering of light that is being detected from outside the focal plane during 2D-STED. Moreover, there is a noticeable increase in Signal-to-Noise ratio during CH-STED. Figure 29, Figure 30 and Figure 32 go further and present profiles of areas in which filaments of a single slice provide higher intensity values, and thus, higher contrast between the imaged object and the background. Figure 33 depicts additional profile analysis of filaments within a Maximum Intensity Projection of the same image stack of the MEF cell sample. This filtering in the axial dimension could be attributed to the consistence of the sub-diffraction area within the lobes of the depletion beam along the Z axis in CH-STED (around 1.8μm in depletion length), focusing on the same spot throughout the scanning of the image, unlike the concentrated depletion in 2D-STED, where the resulting effect occurs in an area half the length in the Z axis (around 1μm in length). The change in intensity power for the depletion beam during imaging (10% for crimson beads and 14-16% for MEF cell sample) was performed to avoid notable photobleaching, as multiple scans of the same region of interest were needed for proper comparison.

Even though z-STED, a commonly used phase mask for axial depletion, is able to provide a higher optical sectioning than 2D-STED, this mask has been proven to suffer from aberrations, sometimes resulting in ghost spots from undepleted excitation lobes, in addition to possible filling of the central zero-intensity area, compromising the depletion effect onto the sample. The CH-STED phase mask, which is a combination of two 2D-STED phase masks, inherits the benefits of low ghost noise and an aberration resistant central zero-intensity area, while providing a superior axial confinement than 2D-STED.

Barbotin et al., (2020) corroborate the analysis of the bi-vortex phase mask implementation regarding successful depletion of background noise unlike in 2D-STED (and 3D-STED), in addition to the low sensitivity to optical aberrations compared to z-STED, especially regarding spherical aberrations which commonly occur during imaging of biological specimens.

Although the consequence of photobleaching derived from the intensity of the depletion beam upon the sample could not be studied, it is encouraged to be pursued in further analysis as the authors suggest the depletion beam should be maximally increased until photodamaging effects are still insignificant, despite any loss in SNR. They express this loss can be recovered by decreasing the rho value of the phase mask. Moreover, they state the intensity of the depletion beam is dispersed along the elongated lobes of the CH-STED phase mask.

5. CONCLUSIONS

In the current thesis, an analysis of the CH-STED phase mask alternative was provided. The program with which the mask is generated has been found reproducible and adaptable, however, troubleshooting must be considered during its initial implementation to any Stimulated Emission Depletion microscope system. The calibration of a specific value, called Unit Circle, is always essential given the variety of optical components between microscope setups that are based on the STED microscopy principle.

The main application and advantage of the CH-STED phase mask over the 2D-STED mask is the improved optical sectioning, despite a slight loss in lateral resolution. Even though z-STED is able to provide a higher axial confinement than 2D-STED, CH-STED inherits the benefits of the phase mask from which it is mainly generated, and still displays satisfactory results in the axial dimension.

Further analysis towards photobleaching is encouraged, since the authors stipulate the power of the depletion beam is dispersed along the elongated lobes of the CH-STED mask, leading to the possibility of using higher powers without immediate damage to the imaging sample.

6. ACKNOWLEDGEMENTS

I would like to dedicate this thesis to the memory of my maternal grandmother, and to my parents, without whom the opportunity to expand my knowledge in science and in life is simply non-existent.

I would also like to thank my wife, Marcela, for her constant aid and support in my life and in my work. Thank you for opening my eyes and helping me see I can accomplish more than what I think I am able to.

Thanks to my immediate supervisor, Elena Tcarenkova, for her willingness to help me and guide me during this process. I hope I have learnt from you thrice as much as you may have from me. I also extend my gratitude to Antonio Pereira, for his disposition to guide my supervisor and me throughout the implementation and analysis of his work. And to professor Pekka Hänninen, for allowing me to be a part of the Laboratory of Biophysics, where you can still feel the Nobel in the air.

Lastly, thank you to my brother and sisters for sharing a laugh with me once in a while, to my wife's family for their incredible help in settling in Finland, and to my BIMA family (especially Anting Li and Monika Vaitkevičiūtė) for their support and coffee breaks.

7. REFERENCES

Abbe, E. 1873. Beiträge zur Theorie des Mikroskops und der mikroskopischen Wahrnehmung. *Archiv f. mikrosk. Anatomie*. 9:413–468. doi:10.1007/BF02956173.

Agha, S., and D. Minkin. 2007. Understanding "Walking the Beam." Stony Brook Laser Teaching Center.

Barbotin, A. 2020. Alignment of an SLM-based STED depletion beam. doi:10.5281/ZENODO.3567748.

Barbotin, A., S. Galiani, I. Urbančič, C. Eggeling, and M.J. Booth. 2019. Adaptive optics allows STED-FCS measurements in the cytoplasm of living cells. *Opt. Express, OE*. 27:23378–23395. doi:10.1364/OE.27.023378.

Barbotin, A., I. Urbančič, S. Galiani, C. Eggeling, and M. Booth. 2020. Background Reduction in STED-FCS Using a Bivortex Phase Mask. *ACS Photonics*. 7:1742–1753. doi:10.1021/acsphotonics.0c00388.

Beater, S., P. Holzmeister, E. Pibiri, B. Lalkens, and P. Tinnefeld. 2014. Choosing dyes for cw-STED nanoscopy using self-assembled nanorulers. *Phys. Chem. Chem. Phys.* 16:6990–6996. doi:10.1039/C4CP00127C.

Betzig, E., G.H. Patterson, R. Sougrat, O.W. Lindwasser, S. Olenych, J.S. Bonifacino, M.W. Davidson, J. Lippincott-Schwartz, and H.F. Hess. 2006. Imaging Intracellular Fluorescent Proteins at Nanometer Resolution. *Science*. 313:1642–1645. doi:10.1126/science.1127344.

Blom, H., and H. Brismar. 2014. STED microscopy: increased resolution for medical research? *Journal of Internal Medicine*. 276:560–578. doi:10.1111/joim.12278.

Cai, B., X. Zhai, Z. Wang, Y. Shen, R. Xu, Z. Smith, Q. Wen, and K. Chu. 2018. Optical volumetric projection for fast 3D imaging through circularly symmetric pupil engineering. *Biomedical Optics Express*. 9:437. doi:10.1364/BOE.9.000437.

Cheng, P.C., and A. Kriete. 1995. Image Contrast in Confocal Light Microscopy. *In* Handbook of Biological Confocal Microscopy. J.B. Pawley, editor. Springer US, Boston, MA. 281–310.

Clausen, M.P., S. Galiani, J.B. de la Serna, M. Fritzsche, J. Chojnacki, K. Gehmlich, B.C. Lagerholm, and C. Eggeling. 2014. Pathways to optical STED microscopy. *NanoBioImaging*. 1. doi:10.2478/nbi-2013-0001.

Diaspro, A., and P. Bianchini. 2013. Two-Photon Excitation Stimulated Emission Depletion Microscopy. *In* Encyclopedia of Biophysics. G.C.K. Roberts, editor. Springer, Berlin, Heidelberg. 2671–2671.

Diaspro, A., P. Bianchini, G. Vicidomini, M. Faretta, P. Ramoino, and C. Usai. 2006. Multi-photon excitation microscopy. *BioMed Eng OnLine*. 5:36. doi:10.1186/1475-925X-5-36.

Dijkstra, R.R.M. 2012. Brightness characterization of single core and core/shell Yb3+,Er3+-doped NaYF4 upconversion nanoparticles & Design and realization of a CW-STED super-resolution microscope setup. University of Twente.

Donnert, G., J. Keller, R. Medda, M.A. Andrei, S.O. Rizzoli, R. Lührmann, R. Jahn, C. Eggeling, and S.W. Hell. 2006. Macromolecular-scale resolution in biological fluorescence microscopy. *Proceedings of the National Academy of Sciences*. 103:11440–11445. doi:10.1073/pnas.0604965103.

Einstein, A. 1916. Strahlungs-Emission und -Absorption nach der Quantentheorie. *Deutsche Physikalische Gesellschaft*. 18:318–323.

Farahani, J., M. Schibler, and L. Bentolila. 2010. Stimulated Emission Depletion (STED) Microscopy: from Theory to Practice. *Microscopy: Science, Technology, Applications and Education*. 2.

Frumker, E., and Y. Silberberg. 2007. Phase and amplitude pulse shaping with two-dimensional phase-only spatial light modulators. *J. Opt. Soc. Am. B*. 24:2940. doi:10.1364/JOSAB.24.002940.

Gemmink. 2017. Myocellular lipid droplets and insulin sensitivity: a microscopy approach. maastricht university.

Göppert-Mayer, M. 1931. Über Elementarakte mit zwei Quantensprüngen. *Annalen der Physik*. 401:273–294. doi:10.1002/andp.19314010303.

Gould, T.J., D. Burke, J. Bewersdorf, and M.J. Booth. 2012. Adaptive optics enables 3D STED microscopy in aberrating specimens. *Opt. Express, OE*. 20:20998–21009. doi:10.1364/OE.20.020998.

Gould, T.J., L.K. Schroeder, P.A. Pellett, and J. Bewersdorf. 2017. STED Microscopy. *In* Fluorescence Microscopy. John Wiley & Sons, Ltd. 321–338.

Gregor, C., F. Grimm, J. Rehman, C.A. Wurm, and A. Egner. 2022. Two-color live-cell STED nanoscopy by click labeling with cell-permeable fluorophores. 2022.09.11.507450. doi:10.1101/2022.09.11.507450.

Grimm, F., S. Nizamov, and V.N. Belov. 2019. Green-Emitting Rhodamine Dyes for Vital Labeling of Cell Organelles Using STED Super-Resolution Microscopy. *ChemBioChem*. 20:2248–2254. doi:10.1002/cbic.201900177.

Haken, H. 1970. Laser Theory. *In* Light and Matter Ic / Licht und Materie Ic. L. Genzel, editor. Springer, Berlin, Heidelberg. 1–304.

Harke, B., P. Bianchini, G. Vicidomini, S. Galiani, and A. Diaspro. 2013. Stimulated Emission Depletion (STED) Microscopy. *In* Encyclopedia of Biophysics. G.C.K. Roberts, editor. Springer, Berlin, Heidelberg. 2470–2475.

Harke, B., C.K. Ullal, J. Keller, and S.W. Hell. 2008. Three-Dimensional Nanoscopy of Colloidal Crystals. *Nano Lett.* 8:1309–1313. doi:10.1021/nl073164n.

Hell, S.W., and J. Wichmann. 1994. Breaking the diffraction resolution limit by stimulated emission: stimulated-emission-depletion fluorescence microscopy. *Opt Lett*. 19:780–782. doi:10.1364/ol.19.000780.

Herman, B. 1998. Fluorescence Microscopy. *Current Protocols in Cell Biology*. 00:4.2.1-4.2.10. doi:10.1002/0471143030.cb0402s13.

Hoang, T.B., G.M. Akselrod, C. Argyropoulos, J. Huang, D.R. Smith, and M.H. Mikkelsen. 2015. Ultrafast spontaneous emission source using plasmonic nanoantennas. *Nat Commun*. 6:7788. doi:10.1038/ncomms8788.

Hotta, J., E. Fron, P. Dedecker, K.P.F. Janssen, C. Li, K. Müllen, B. Harke, J. Bückers, S.W. Hell, and J. Hofkens. 2010. Spectroscopic Rationale for Efficient Stimulated-

Emission Depletion Microscopy Fluorophores. *J. Am. Chem. Soc.* 132:5021–5023. doi:10.1021/ja100079w.

Huang, B., M. Bates, and X. Zhuang. 2009. Super-resolution fluorescence microscopy. *Annu Rev Biochem*. 78:993–1016. doi:10.1146/annurev.biochem.77.061906.092014.

Icha, J., M. Weber, J.C. Waters, and C. Norden. 2017. Phototoxicity in live fluorescence microscopy, and how to avoid it. *BioEssays*. 39:1700003. doi:10.1002/bies.201700003.

Jacquemet, G., A.F. Carisey, H. Hamidi, R. Henriques, and C. Leterrier. 2020. The cell biologist's guide to super-resolution microscopy. *Journal of Cell Science*. 133:jcs240713. doi:10.1242/jcs.240713.

Keller, H.E. 1995. Objective Lenses for Confocal Microscopy. *In* Handbook of Biological Confocal Microscopy. J.B. Pawley, editor. Springer US, Boston, MA. 111–126.

Keller, J., A. Schönle, and S.W. Hell. 2007. Efficient fluorescence inhibition patterns for RESOLFT microscopy. *Opt Express*. 15:3361–3371. doi:10.1364/oe.15.003361.

Klar, T.A., and S.W. Hell. 1999. Subdiffraction resolution in far-field fluorescence microscopy. *Opt. Lett., OL*. 24:954–956. doi:10.1364/OL.24.000954.

Krainak, M.A. 2005. Photoionization of trapped carriers in avalanche photodiodes to reduce afterpulsing during Geiger-mode photon counting. *In* (CLEO). Conference on Lasers and Electro-Optics, 2005. IEEE, Baltimore, MD, USA. 588-590 Vol. 1.

Kuang, C., W. Zhao, and G. Wang. 2010. Far-field optical nanoscopy based on continuous wave laser stimulated emission depletion. *Review of Scientific Instruments*. 81:053709. doi:10.1063/1.3432001.

Lakowicz, J.R. ed. . 2006. Principles of Fluorescence Spectroscopy. Springer US, Boston, MA.

Latychevskaia, T. 2019. Lateral and axial resolution criteria in incoherent and coherent optics and holography, near- and far-field regimes. *Appl. Opt.* 58:3597. doi:10.1364/AO.58.003597.

Lenz, M.O., and J. Tønnesen. 2019. Considerations for Imaging and Analyzing Neural Structures by STED Microscopy. *In* Glutamate Receptors: Methods and Protocols. C. Burger and M.J. Velardo, editors. Springer, New York, NY. 29–46.

Li, Y., H. Zhou, X. Liu, Y. Li, and L. Wang. 2018. Effects of aberrations on effective point spread function in STED microscopy. *Appl. Opt., AO*. 57:4164–4170. doi:10.1364/AO.57.004164.

Liang, Y., Y. Jian, X. Chen, G. Wu, E. Wu, and H. Zeng. 2011. Room-Temperature Single-Photon Detector Based on InGaAs/InP Avalanche Photodiode With Multichannel Counting Ability. *Photonics Technology Letters, IEEE*. 23:115–117. doi:10.1109/LPT.2010.2092756.

Liang, Y., and H. Zeng. 2014. Single-photon detection and its applications. *Sci. China Phys. Mech. Astron.* 57:1218–1232. doi:10.1007/s11433-014-5450-0.

Likhotkin, I., R. Lincoln, M.L. Bossi, A.N. Butkevich, and S.W. Hell. 2023. Photoactivatable Large Stokes Shift Fluorophores for Multicolor Nanoscopy. *J. Am. Chem. Soc.* 145:1530–1534. doi:10.1021/jacs.2c12567.

Möckl, L., D.C. Lamb, and C. Bräuchle. 2014. Super-resolved Fluorescence Microscopy: Nobel Prize in Chemistry 2014 for Eric Betzig, Stefan Hell, and William E. Moerner. *Angewandte Chemie International Edition*. 53:13972–13977. doi:10.1002/anie.201410265.

Mol, F.N., and R. Vlijm. 2022. Automated STED nanoscopy for high-throughput imaging of cellular structures. 2022.09.29.510126. doi:10.1101/2022.09.29.510126.

Moreno, I., J.A. Davis, T.M. Hernandez, D.M. Cottrell, and D. Sand. 2012. Complete polarization control of light from a liquid crystal spatial light modulator. *Opt. Express*. 20:364. doi:10.1364/OE.20.000364.

Müller, T., C. Schumann, and A. Kraegeloh. 2012. STED Microscopy and its Applications: New Insights into Cellular Processes on the Nanoscale. *ChemPhysChem*. 13:1986–2000. doi:10.1002/cphc.201100986.

Murphy, D.B. 2002. Fundamentals of Light Microscopy and Electronic Imaging. John Wiley & Sons. 387 pp.

Pawley, J.B. 2006. Points, Pixels, and Gray Levels: Digitizing Image Data. *In* Handbook Of Biological Confocal Microscopy. J.B. Pawley, editor. Springer US, Boston, MA. 59–79.

Pereira, A., M. Sousa, A.C. Almeida, L.T. Ferreira, A.R. Costa, M. Novais-Cruz, C. Ferrás, M.M. Sousa, P. Sampaio, M. Belsley, and H. Maiato. 2019. Coherent-hybrid STED: high contrast sub-diffraction imaging using a bi-vortex depletion beam. *Opt Express*. 27:8092–8111. doi:10.1364/OE.27.008092.

Pereira, A.J., M. Sousa, A.C. Almeida, L.T. Ferreira, A.R. Costa, M. Novais-Cruz, C. Ferrás, M.M. Sousa, P. Sampaio, M. Belsley, and H. Maiato. 2018. Coherent-hybrid STED: a tunable photo-physical pinhole for super-resolution imaging at high contrast. 381343. doi:10.1101/381343.

Polyakov, S.V. 2013. Chapter 3 - Photomultiplier Tubes. *In* Experimental Methods in the Physical Sciences. A. Migdall, S.V. Polyakov, J. Fan, and J.C. Bienfang, editors. Academic Press. 69–82.

Reuss, M., J. Engelhardt, and S.W. Hell. 2010. Birefringent device converts a standard scanning microscope into a STED microscope that also maps molecular orientation. *Opt. Express, OE*. 18:1049–1058. doi:10.1364/OE.18.001049.

Reuss, M., F. Fördős, H. Blom, O. Öktem, B. Högberg, and H. Brismar. 2017. Measuring true localization accuracy in super resolution microscopy with DNA-origami nanostructures. *New J. Phys.* 19:025013. doi:10.1088/1367-2630/aa5f74.

Sanderson, M.J., I. Smith, I. Parker, and M.D. Bootman. 2014. Fluorescence Microscopy. *Cold Spring Harb Protoc*. 2014:pdb.top071795. doi:10.1101/pdb.top071795.

Schweizer, T., H. Kubach, and T. Koch. 2021. Investigations to characterize the interactions of light radiation, engine operating media and fluorescence tracers for the use of qualitative light-induced fluorescence in engine systems. *Automotive and Engine Technology*. 6:1–13. doi:10.1007/s41104-021-00092-3.

Semwogerere, D., and E.R. Weeks. 2008. Confocal Microscopy. Routledge Handbooks Online.

Sheppard, C., and Z. Hegedus. 1988. Axial behavior of pupil-plane filters. *Journal of The Optical Society of America A-optics Image Science and Vision - J OPT SOC AM A-OPT IMAGE SCI*. 5. doi:10.1364/JOSAA.5.000643.

Singh, K., A.K. Gupta, S. Khare, N. Dixit, and K. Pant eds. . 2021. ICOL-2019: Proceedings of the International Conference on Optics and Electro-Optics, Dehradun, India. 258. Springer Singapore, Singapore.

Staudt, T., A. Engler, E. Rittweger, B. Harke, J. Engelhardt, and S.W. Hell. 2011. Far-field optical nanoscopy with reduced number of state transition cycles. *Opt. Express, OE*. 19:5644–5657. doi:10.1364/OE.19.005644.

Tortarolo, G., A. Zunino, F. Fersini, M. Castello, S. Piazza, C. Sheppard, P. Bianchini, A. Diaspro, S. Koho, and G. Vicidomini. 2022. Focus image scanning microscopy for sharp and gentle super-resolved microscopy. *Nature Communications*. 13:7723. doi:10.1038/s41467-022-35333-y.

Verdaasdonk, J.S., A.D. Stephens, J. Haase, and K. Bloom. 2014. Bending the Rules: Widefield Microscopy and the Abbe Limit of Resolution. *Journal of Cellular Physiology*. 229:132–138. doi:10.1002/jcp.24439.

Vicidomini, G., P. Bianchini, and A. Diaspro. 2018. STED super-resolved microscopy. *Nat Methods*. 15:173–182. doi:10.1038/nmeth.4593.

Vicidomini, G., and G. Moneron. 2013. Gated Stimulated Emission Depletion Microscopy (g-STED). *In* Encyclopedia of Biophysics. G.C.K. Roberts, editor. Springer, Berlin, Heidelberg. 888–889.

Vicidomini, G., G. Moneron, K.Y. Han, V. Westphal, H. Ta, M. Reuss, J. Engelhardt, C. Eggeling, and S.W. Hell. 2011. Sharper low-power STED nanoscopy by time gating. *Nat Methods*. 8:571–573. doi:10.1038/nmeth.1624.

Wahl, M. 2014. Time-Correlated Single Photon Counting.

Wang, B., J. Shi, T. Zhang, X. Xu, Y. Cao, and X. Li. 2017. Improved lateral resolution with an annular vortex depletion beam in STED microscopy. *Opt Lett*. 42:4885–4888. doi:10.1364/OL.42.004885.

Wildanger, D., R. Medda, L. Kastrup, and S. w. Hell. 2009. A compact STED microscope providing 3D nanoscale resolution. *Journal of Microscopy*. 236:35–43. doi:10.1111/j.1365-2818.2009.03188.x.

Willig, K.I., B. Harke, R. Medda, and S.W. Hell. 2007. STED microscopy with continuous wave beams. *Nat Methods*. 4:915–918. doi:10.1038/nmeth1108.

Wilson, T. 2011. Optical sectioning in fluorescence microscopy: OPTICAL SECTIONING IN FLUORESCENCE MICROSCOPY. *Journal of Microscopy*. 242:111–116. doi:10.1111/j.1365-2818.2010.03457.x.

Wu, W., X. Shan, Y. Long, J. Ma, K. Huang, M. Yan, Y. Liang, and H. Zeng. 2023. Free-Running Single-Photon Detection via GHz Gated InGaAs/InP APD for High Time Resolution and Count Rate up to 500 Mcount/s. *Micromachines*. 14:437. doi:10.3390/mi14020437.

Wu, Y., X. Wu, R. Lu, M. Li, L. Toro, and E. Stefani. 2016. Super-Resolution Light Microscopy: Stimulated Emission Depletion and Ground-State Depletion. *In* Encyclopedia of Cell Biology. R.A. Bradshaw and P.D. Stahl, editors. Academic Press, Waltham. 76–85.

Wurm, C.A., K. Kolmakov, F. Göttfert, H. Ta, M. Bossi, H. Schill, S. Berning, S. Jakobs, G. Donnert, V.N. Belov, and S.W. Hell. 2012. Novel red fluorophores with superior performance in STED microscopy. *Optical Nanoscopy*. 1:7. doi:10.1186/2192-2853-1-7.

Yan, W., Y. Huang, L. Wang, J. Li, Y. Guo, Z. Yang, and J. Qu. 2022. Multi-Color Two-Photon Microscopic Imaging Based on a Single-Wavelength Excitation. *Biosensors*. 12:307. doi:10.3390/bios12050307.

Young, M. 2003. Imaging Optics. *In* Encyclopedia of Physical Science and Technology (Third Edition). R.A. Meyers, editor. Academic Press, New York. 645–660.

Yuan, Z.L., B.E. Kardynal, A.W. Sharpe, and A.J. Shields. 2007. High speed single photon detection in the near-infrared. *Appl. Phys. Lett.* 91:041114. doi:10.1063/1.2760135.

Zhang, J., X. Gao, L. Wang, Y. Guo, Y. Zhu, Z. Yang, W. Yan, and J. Qu. 2021. Low-Power Two-Color Stimulated Emission Depletion Microscopy for Live Cell Imaging. *Biosensors*. 11:330. doi:10.3390/bios11090330.

8. APPENDICES

The R script used to determine the coefficients of the fitting of the parabolic approximation to the profiles drawn at the focal plane of the gold beads is shown as follows:

```
###############################
#General preparations
###############################


#clean env
rm(list = ls())
#read all csv from the folder
setwd(‘/Users/rfadz/Desktop/cab_work/particle003’)
library(‘data.table’)
#load the list of csv names
temp = list.files(pattern=”*.csv”,full.names=TRUE)
temp #check csv names
#load data
myfiles = lapply(temp, read.delim, sep =’,’)
#how many files
plot_setup<-length(temp)
#to store c coefficient
neighborhood=5
#coefAprox <- c()
result.data = data.frame()


###############################
#process for all csv files
###############################

i=0 #just counter for loop
for (n in myfiles) {

  i=i+1
  par(mfrow=c(3,1))

  #take the value rho from file name
  rho=substring(temp[i],26,31)

  #open file where we save results   do not forget to close # dev.off()
  # filename.pdf <- gsub(" ", "",paste('parabolicApprox/','a_',rho,'.pdf'))
  # pdf(file = filename.pdf)

  psf <- myfiles[[i]]


  #################################
```

```
  tt<- psf$Gray_Value
  ee<-which(diff(sign(diff(tt)))==-2)+1


  ### normalization
  psf$Gray_Value <- psf$Gray_Value/max (psf$Gray_Value)

  par(mfrow=c(3,1))

  plot(psf$Distance_.microns,psf$Gray_Value,type = "b", xlim=c(0,
max(psf$Distance_.microns+0.2)), col=1, pch=16, cex=1, lty=1, xlab = "Distance
(um)", ylab = "Intensity",ylim=c(2500, max(psf$Gray_Value+1000)))

  points(psf$Distance_.microns[ee], psf$Gray_Value[ee], cex = 2, pch = 1, col
="red")

  #remove indexes of those maximum whose ray_Value is twice smaller than max
  highest.pick <- ee[psf$Gray_Value[ee]>=(max(psf$Gray_Value)*0.9)]
  locmax <- psf$Gray_Value[highest.pick[1]]

  #higlight peaks marked on the plot
  points(psf$Distance_.microns[highest.pick], psf$Gray_Value[highest.pick], cex =
3, pch = 1, col ="blue")

  #search middle between peaks
  mid.point = highest.pick[1] + (ceiling(highest.pick[2]-highest.pick[1]))/2

  #add mid.point to plot with data
  points(psf$Distance_.microns[mid.point], psf$Gray_Value[mid.point], cex = 2, pch
= 1, col ="green")

  legend("topright", legend=c("Local Maxs", "Signif. Max", "Midpoint of data"),
         col=c("red", "blue","green"), lty=1:1, box.lty=0, cex=1)

  #################################


  #################################
  #selection of middle range of the PSF and plot
  ################################

  datalength<-length(psf$Distance_.microns)



  #minimum.psf<-psf[((mid.point-neighborhood):(mid.point+neighborhood)),]
  minimum.psf<-psf[highest.pick[1]:highest.pick[2],]
  plot(minimum.psf$Distance_.microns,minimum.psf$Gray_Value,col=1, pch=16, cex=1,
lty=1,type = "b",xlab = "Distance (um)", ylab = "Intensity",
       ylim=c(2500, max(psf$Gray_Value+1000)))

  points(psf$Distance_.microns[mid.point], psf$Gray_Value[mid.point], cex = 2, pch
= 1, col ="green")



  #select data within neighborhood
  selectedData<-psf[((mid.point-neighborhood):(mid.point+neighborhood)),]
  #selectedData<-rightsideMaxPSF
  #grayValue=a+b*distanceInMicr+c*distanceInMicr^2
  #Z=distanceInMicr^2
  selectedData$Z=selectedData$Distance_.micron^2
  output=lm(selectedData$Gray_Value~selectedData$Distance_.microns+selectedData$Z)

  output
  a=output$coefficients[1]
  b=output$coefficients[2]
  c=output$coefficients[3]
```

```
  # to store c coefficient
  #coefAprox[n] <- c

  selectedData$outputPrediction=a+b*selectedData$Distance_.microns+c*selectedData$Z

  # plot selected part and fitting
  plot(selectedData$Distance_.microns,selectedData$Gray_Value,col=1, pch=16, cex=1,
lty=1,type = "b",xlab = "Distance (um)",
       ylab = "Intensity", xlim=c(min(selectedData$Distance_.microns),
max(selectedData$Distance_.microns)), ylim=c(2500, max(psf$Gray_Value+1000)))

  par(new=TRUE)
  plot(selectedData$Distance_.microns,selectedData$outputPrediction, col=2,
pch="+", type = "b", xlab="",ylab = "Intensity",
xlim=c(min(selectedData$Distance_.microns), max(selectedData$Distance_.microns))
,ylim=c(2500, max(psf$Gray_Value+1000)))

  legend("topright", legend=c("Experimental", "Parabolic"), col=c("black", "red"),
lty=1:1, box.lty=0, cex=1,
        )
  #name all graphs

  rhoValue <- gsub(" ", "", paste(substring(rho,4,4), '.', substring(rho,5,7)))

  mtext(paste('Rho = ', rhoValue), side = 3, line = - 2, outer = TRUE)



  #Use result.data to display all coefficients vs rho values
  result <- list(rho=substring(rho,4,), coefC=c)
  result.data = rbind(result.data, result)}

#dev.off()

}


write.csv(result.data, file = "parabolicApprox/result.csv")

#take rho and convert from string to number
result.data$rho1 <- as.double(gsub(" ", "",
paste(substring(result.data$rho,1,1),'.', substring(result.data$rho,2,3))))


#plot rho to coefAprox
par(mfrow=c(1,1))

plot(result.data$rho1, result.data$coefC,col=20,pch="o",type = "b", xlab = "rho",
   ylab = "c")
grid(nx = NULL, ny = NULL, col = "lightgray", lty = "dotted")


summary(output)

#####################
```